

High-order alloharmonics produced by nonperiodic drivers

M. S. Pirozhkova^{1*}, K. Ogura^{1*}, A. Sagisaka¹, T. Zh. Esirkepov¹, A. Ya. Faenov^{2†}, T. A. Pikuz², H. Kotaki¹, Y. Hayashi¹, Y. Fukuda¹, J. K. Koga¹, S. V. Bulanov^{1,3}, H. Daido⁴, N. Hasegawa¹, M. Ishino¹, M. Nishikino¹, M. Koike¹, T. Kawachi¹, H. Kiriya¹, M. Kando¹, D. Neely^{5,6†}, A. S. Pirozhkov¹

*These authors contributed equally

e-mail: pirozhkov.alexander @ qst.go.jp

31 May 2023

- 1 Kansai Photon Science Institute, National Institutes for Quantum Science and Technology, 8-1-7 Umemidai, Kizugawa, Kyoto 619-0215, Japan
- 2 Institute for Open and Transdisciplinary Research Initiatives, Osaka University, Suita, Osaka 565-0871, Japan
- 3 Institute of Physics of the Czech Academy of Sciences, Extreme Light Infrastructure Beamlines Project, Na Slovance 2, 18221 Prague, Czech Republic
- 4 Institute for Laser Technology, 2-6 Yamada-oka, Suita, Osaka 565-0871, Japan
- 5 Central Laser Facility, Rutherford Appleton Laboratory, STFC, Chilton, Didcot, Oxon OX11 0QX, United Kingdom
- 6 Department of Physics, SUPA, University of Strathclyde, Glasgow G4 0NG, United Kingdom

† Deceased

Abstract: High-order harmonics are ubiquitous in nature and present in electromagnetic^{1,2}, acoustic, and gravitational waves^{3,4}. They are generated by periodic nonlinear processes or periodic high-frequency pulses^{5,6}. However, this periodicity is often inexact, such as that in chirped (frequency-swept) optical waveforms⁷ or interactions with nonstationary matter – for instance, reflection from accelerating mirrors. Spectra observed in such cases⁸⁻¹¹ contain complicated sets of harmonic-like fringes. We encountered such fringes in our experiment on coherent extreme ultraviolet generation via BISER^{12,13}, and could not interpret them using currently available knowledge. Here, we present a comprehensive theory based on interference of harmonics with different orders fully explaining the formation of these fringes, which we call *alloharmonics*. Like atomic spectra, the complex alloharmonic spectra depend on several integer numbers and bear a unique imprint of the emission process, which the theory can decipher, avoiding confusion or misinterpretation. We also demonstrate the alloharmonics in simulations^{14,15} of gravitational waves emitted by binary black hole mergers. Further, we predict the presence of alloharmonics in the radio spectra of pulsars and in optical frequency combs, and propose their use for measurement of extremely small accelerations necessary for testing gravity theories. The alloharmonics phenomenon generalizes classical harmonics and is critical in research fields such as laser mode locking, frequency comb generation, attosecond pulse generation, pulsar studies, and future gravitational wave spectroscopy.

Introduction

Harmonics in the frequency domain. High-order harmonics are phase-coherent spectra with distinct components separated by a frequency called the base, fundamental or driver frequency. Harmonics appear in many processes, such as laser-driven harmonic generation in ionizing gases¹ and from plasma surfaces², and burst intensification by singularity emitting radiation (BISER)^{12,13}. Similar spectra appear in the most accurate absolute frequency references^{16,17} – optical frequency combs, i.e., spectra of highly periodic optical pulse trains generated by a laser pulse bouncing inside stabilized cavities. Harmonics are also present in acoustic and gravitational waves^{3,4}. Harmonic components have angular frequencies $\omega_n = n\omega_0 + \omega_{\text{CEO}} = (n + \delta n)\omega_0$, where the harmonic order n is a positive integer, ω_0 is the base frequency, $0 \leq \delta n < 1$, $\omega_{\text{CEO}} = \delta n\omega_0 = \omega_0 \Delta\varphi_{\text{CEO}}/2\pi$ is the carrier-envelope offset corresponding to the pulse-to-pulse change $\Delta\varphi_{\text{CEO}}$ of the carrier wave phase in the pulse train. If all harmonic orders are present, the harmonic fringe separation is $\Delta\omega = \omega_{n+1} - \omega_n = \omega_0$. Not all orders may be present due to specific symmetries; for example, gas harmonics driven by multicycle lasers contain only odd orders with a separation of $\Delta\omega = 2\omega_0$ due to field-reversal symmetry, while plasma surface harmonics may contain all ($\Delta\omega = \omega_0$), odd ($\Delta\omega = 2\omega_0$), or even ($\Delta\omega = 2\omega_0$) orders depending on the incidence angle and polarization^{18,19}. Importantly, in all cases, the harmonic separation is an integer *multiple* of the base frequency.

Harmonics in the time domain. Equivalently, harmonics can be considered in the time domain connected with the spectral domain via the Fourier transform. The presence of periodically spaced spectral components with separation $\Delta\omega$ corresponds to coherent periodically spaced pulses in time separated by $\Delta T = 2\pi/\Delta\omega$. For harmonics spaced by one driver frequency ($\Delta\omega = \omega_0$), the pulse time separation is one driver cycle $\Delta T = 2\pi/\omega_0 = T_0$, while for $\Delta\omega = 2\omega_0$, the time separation $\Delta T = T_0/2$ is half the driver cycle. In a frequency comb, the time separation $\Delta T = 2\pi/\omega_0 = 1/\nu_{\text{rep}}$ is the inverse of the pulse train repetition rate. In many practical cases, the harmonics are nearly phase-matched, and thus, their Fourier synthesis gives sharp pulses in the time domain with durations that are considerably shorter than the time separation ΔT . This approach generates femtosecond laser pulses – in research, technology, and medicine – employing $\sim 10^5$ to 10^7 harmonics with MHz or GHz repetition rate frequency combs, and attosecond pulses – the fastest probes available at present – employing several to several tens of harmonics with various generation mechanisms²⁰⁻²³.

Nonperiodic drivers. The harmonic-generating driver frequency is – or assumed to be – constant. Yet, there are also many important examples of inexactly periodic drivers in various research fields. For instance, laser pulse frequency sweep is used to generate the highest laser powers via chirped pulse amplification⁷. Laser frequency can also change over time due to propagation in ionizing medium^{24,25}, photon acceleration^{26,27}, and time-varying Doppler shift upon nonlinear reflection from accelerating mirror⁸⁻¹¹. The frequency of an intense laser gradually downshifts – and can decrease by a large factor²⁸ – in the nonlinear depletion process^{29,30}, where the laser pulse propagating in tenuous plasma transfers its energy to plasma waves, which power laser electron accelerators³¹, BISER^{12,13} and other bright x-ray sources³², and produce intense single-cycle infrared pulses³³. The repetition rates of the pulse trains forming frequency combs change if the laser cavity parameters drift or are intentionally varied. Binary black holes rotate with gradual accelerations as they inspiral^{4,34}. The rotation frequencies of pulsars slowly decrease during spin-downs^{35,36} but increase during glitches³⁷. The high-frequency spectra generated by such nonperiodic drivers differ in various ways from classical harmonics. For instance, there can be

broadening of each individual harmonic bandwidth, which increases with harmonic order³⁸. Or, harmonics and half-integer harmonics can be present¹¹. Or, the harmonic structure can be lost completely, being replaced with harmonic-like fringes¹⁰. In each individual case, it has been correctly reasoned that the observed spectral features are determined by driver nonperiodicity, and corresponding nonperiodic pulse train models have been proposed.

The puzzle. However, like atomic spectra without quantum mechanics, our experimental spectra produced via the BISER mechanism were inexplicable by currently available concepts and models. Even the driver frequency, not mentioning its nonperiodicity parameters, could not be determined. Most importantly, clear physical understanding and governing equations were absent.

Gap of knowledge which will be addressed and importance. Here, we develop a theory of coherent spectra formation in nonperiodic cases. The theory explains our experimental data and explains why they are inexplicable without it. We show that in an important case of small nonperiodicity, normal harmonic fringes with gradually increasing bandwidth are formed at low harmonic orders, while, at higher frequencies, additional spectral fringes (*alloharmonics*) are produced by the spectral interference of same-frequency but different harmonic orders from different pulses of the train, resulting in spectral fringe separations approximately equal to various integer *fractions* of the base frequency. With this theory, we predict the frequencies at which alloharmonics appear in the spectra, their fringe spacing, and required resolving power *and* bandwidth to correctly measure these fringes. Our theory also allows derivation of the parameters of driver nonperiodicity from measured spectra, which we do for our BISER data. The theory is widely applicable to all nonperiodic harmonic-generating drivers. We analyse gravitational wave spectra from previously published state-of-the-art numerical relativity simulations^{14,15} of inspiralling binary black holes and obtain results consistent with our theory. We also predict important implications for frequency comb spectroscopy, where the alloharmonic concept allows extension into regimes with moving and accelerating laser cavity mirrors, and pulsar studies, in both of which previously unavailable nonperiodicity properties can be derived from alloharmonic observations. We argue that unaccounted-for alloharmonics can cause a lot of confusion and misinterpretation of observations in laser labs and astrophysics.

Results

Experiment inexplicable. In our experiment we generated coherent extreme ultraviolet pulses via the BISER mechanism, where an intense laser pulse propagating in tenuous plasma produced structurally stable relativistic singularities. These nanoscale-size sources emitted bright BISER radiation with the spectrum shown in Fig. 1a. Ext. Fig. 1 shows the corresponding raw data and Ext. Fig. 2 shows the spectrograph calibration and resolving power. The spectrum has distinct fringe periods at different photon energies, e.g., $\Delta\omega \approx \omega_X$ at ~ 45 and 66 eV, while $\Delta\omega \approx \omega_X/2$ at ~ 58 eV, corresponding to some photon energy $\hbar\omega_X \approx 0.63$ eV; here \hbar is the reduced Planck constant. Note that these fringe periods differ from the laser photon energy, $\hbar\omega_L = 1.53$ eV. Furthermore, the positions of the antinodes correspond to approximately $n \times 0.63$ eV and $(n + 0.5) \times 0.63$ eV at ~ 45 and 66 eV, respectively. Observing this spectrum in narrow spectral ranges would give an incorrect impression of some harmonics, with the base frequency and carrier-envelope offset depending on the observation region: $\omega_n \approx n\omega_X$, $\omega_n \approx n\omega_X/2$, and $\omega_n \approx (n + 0.5)\omega_X$, respectively. The entire spectrum cannot be interpreted in terms of harmonics. Knowing that the intense laser frequency gradually and continuously downshifts in tenuous plasma and

the local frequency can change due to plasma dispersion and photon acceleration, and based on the existing models, we inferred that a nonperiodic driver generated the puzzling spectrum. However, the observed spectral features remained unexplained and the parameters of nonperiodicity remained unknown. A complication like with astrophysical drivers was that at the instant of BISER generation the laser frequency, which in other laser experiments serves as a reliable reference, was unknown.

Alloharmonics concept. A hint can be derived from the filtered (local) Fourier transforms, Fig. 1**b1-3**: the discrete peaks demonstrate time separations that determine the spectral fringe periodicity in the corresponding spectral intervals. Thus, like harmonic spectra, the spectral fringes in the experiment resulted from spectral interference of coherent time-separated pulses, but, in contrast to harmonics, the time separations corresponded to a nonperiodic pulse train, apparent from the displacements of the peaks from the vertical dashed lines. However, the spectral interference requires equivalence (overlap) of frequencies of different pulses, which seems impossible due to the pulse-to-pulse base frequency change. To explain the experimental observations, we propose the alloharmonic concept, i.e., the spectral interference of the harmonic order n from pulse number m (instantaneous frequency ω_m) with *another* harmonic $n + \Delta n$ from pulse $m + \Delta m$ (instantaneous frequency $\omega_{m+\Delta m}$), with the interharmonic separation Δn and pulse separation $\Delta m > 0$. The frequency equivalence gives *the alloharmonic equation*:

$$(1) \quad (n + \delta n)\omega_m = (n + \delta n + \Delta n)\omega_{m+\Delta m}.$$

This is a linear equation for n yielding a nontrivial solution for $\omega_m \neq \omega_{m+\Delta m}$. The alloharmonic fringes appear at corresponding frequencies $\omega_A = (n + \delta n)\omega_m$. For slow frequency variation, $\omega_m \approx \omega_{m+\Delta m}$, the frequency difference $(n + \delta n)(\omega_m - \omega_{m+\Delta m})$ is small for low orders n , thus, (1) can be approximately satisfied for $\Delta n = 0$, representing the harmonic solution. At higher orders, this frequency difference becomes large and the harmonics vanish, while the alloharmonic solution remains, with $\Delta n \neq 0$.

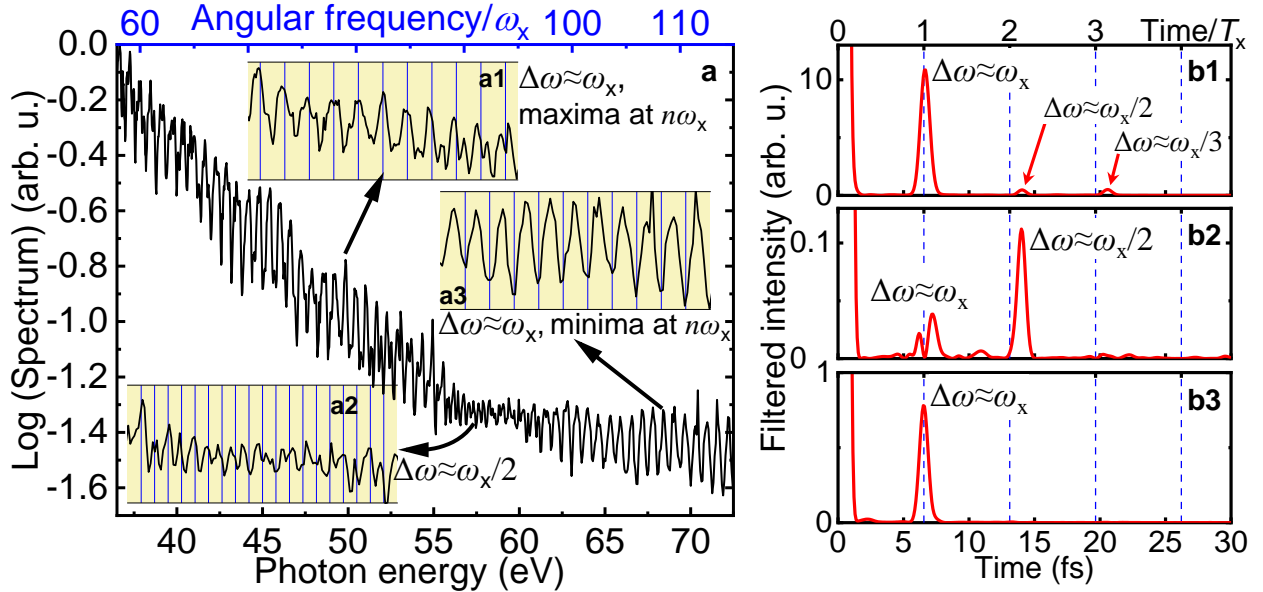


Fig. 1. Coherent extreme ultraviolet spectrum generated by a gradually-frequency-downshifting relativistic-irradiance laser pulse via the burst intensification by singularity emitting radiation (BISER)

mechanism. a, Experimental BISER spectrum. The insets **a1-a3** show spectral regions with fringe separations $\Delta\omega \approx \omega_x, \omega_x/2$, and ω_x , respectively, with $\hbar\omega_x \approx 0.63$ eV; vertical lines indicate integer multiples of the corresponding fringe periods, $n\Delta\omega$. Note that the spectral fringe period in **a2** differs from that in **a1** and **a3**, and all the fringe periods differ from the initial laser photon energy $\hbar\omega_L \approx 1.53$ eV. Also note that at frequencies $n\omega_x$ the spectrum exhibits antinodes in **a1** but nodes in **a3**. **b1-b3**, Intensities of filtered (local) Fourier transforms of the experimental spectrum, with applied Gaussian filters with a half-width of 2 eV at $1/e^2$ and centres at $\hbar\omega = 45, 58$, and 66 eV, corresponding to the insets **a1-a3**, respectively. Blue vertical dashed lines denote periods corresponding to ω_x .

Theory and model. Fourier transform of the spectrum, such as shown in Fig. **1b1-3**, does not include phase and thus cannot reconstruct the true pulse train in the time domain – in particular, while the existing pulse separations can be obtained, their relative positions cannot. A model of high-order harmonics including phase has been used, for example, in Ref.⁵. Its generalization to a nonconstant-driver-frequency case is:

$$(2) \quad E(t) = A_\tau(t) \sum_n a_n \cos[(n + \delta n)\Phi(t) + \phi_n].$$

Here, $E(t)$ is the amplitude (electromagnetic field, gravitational strain, etc.), t is the time, $A_\tau(t)$ is the envelope with duration τ , a_n is the n^{th} harmonic amplitude, ϕ_n is the spectral phase characterizing phase matching, $\Phi(t)$ is the driver phase, $\omega(t) = \frac{d\Phi(t)}{dt}$ is the instantaneous driver frequency. The model and derivation of equations are in Supplemental Note 1. According to the known property of this model, for a reasonably small phase mismatch ($\phi_{n+1} - \phi_n$), the amplitude $E(t)$ is close to zero everywhere except for several sharp pulses (Fig. **2a**), with the positions t_m satisfying

$$(3) \quad \Phi(t_m) = 2\pi m - (\phi_{n+1} - \phi_n) \approx 2\pi m,$$

where m is the pulse number: $m = 0$ is the main pulse at $t = 0$, while $m = \pm 1, \pm 2, \dots$ are satellites before ("–") and after ("+") this pulse. Periodic drivers, $\omega(t) = \omega_0$, produce equidistant pulses at $t_m = mT_0$ and equidistant harmonics with frequency separations of $\Delta\omega = 2\pi/T_0 = \omega_0$ due to the interference between the equal frequencies $(n + \delta n)\omega_0$ of all the pulses. For nonperiodic drivers, Eq. (3) gives nonperiodic pulse train, i.e., nonequidistant pulses in the time domain, with the base frequency depending on the pulse number: $\omega_m = \omega(t_m)$. In many important cases the nonperiodicity is small and the nonlinear driver phase $\Phi(t)$ can be approximated as

$$(4) \quad \Phi(t) = \omega_0 t \left(1 + \alpha \frac{t}{T_0} + \beta \left(\frac{t}{T_0} \right)^2 + \gamma \left(\frac{t}{T_0} \right)^3 + \delta \left(\frac{t}{T_0} \right)^4 + \dots \right)$$

with dimensionless nonperiodicity (chirp) parameters $\alpha, \beta, \gamma, \delta, \dots \ll 1$.

The alloharmonic concept allows exploring previously unknown properties of the model, exemplifying them by a quadratic phase case, $\Phi(t) = \omega_0 t \left(1 + \alpha \frac{t}{T_0} \right)$ (Fig. 2), for which Eq. (3) yields pulses at $t_m = \frac{\sqrt{1+4m\alpha}-1}{2\alpha} T_0 \approx (m - \alpha m^2 + 2\alpha^2 m^3 + \dots) T_0$ with frequencies $\omega_m = \omega(t_m) = \omega_0 \sqrt{1+4m\alpha} \approx (1 + 2m\alpha + \dots) \omega_0$ (Fig. **2a**). The overall spectrum, i.e., the Fourier transform of the field $E(t)$, is complicated (Fig. **2b**). At relatively low frequencies (below $\sim 25\omega_0$), there are harmonics with frequencies $(n + \delta n)\omega_0$ (Fig. **2c1**) that appear "normally", i.e., via spectral interference of the same-order harmonics of different pulses, thus forming the $\Delta n = 0$ series, i.e., an approximate harmonic solution of Eq. (1). These harmonics

differ from ideal (periodic-driver) harmonics as they show gradually decreasing amplitudes, increasing widths, and decreasing fringe visibility with increasing harmonic order.

However, at higher frequencies, the fringe visibility increases again, with different fringe separations (e.g., $\Delta\omega \approx \omega_0/6$, $\omega_0/3$ and $\omega_0/1$; Fig. 2c2-c4, respectively). These are the alloharmonics; they appear at sets of frequencies which satisfy Eq. (1) for different integer values of m , $\Delta m > 0$, $\Delta n \neq 0$. Eq. (1) can be illustrated by a moiré pattern (Fig. 2d): like a vernier scale, the two different combs match at certain different line numbers (harmonic orders), thus providing frequency equivalence necessary for the spectral interference. Such moiré patterns differ for each $(m, \Delta m)$ pair; thus, alloharmonics appear at many different frequencies ω_A . For the quadratic phase, Eq. (1) yields:

$$(5) \quad \frac{\omega_A}{\omega_0} \approx -\frac{1}{2\alpha} \frac{\Delta n}{\Delta m} - \left[3\Delta n \left(\frac{m}{\Delta m} + \frac{1}{2} \right) \right].$$

More precise and general equations are in Supplemental Note 1. The first term is dominant for $\alpha \ll 1$, resulting in several closely spaced frequency series with equal ratios $\Delta n/\Delta m$ (dashed vertical lines in Fig. 2b, c). The alloharmonic fringe separations for the quadratic phase are

$$(6) \quad \Delta\omega = \frac{2\pi}{t_{m+\Delta m} - t_m} = -\frac{2\alpha}{\sqrt{1+4m\alpha} - \sqrt{1+4(m+\Delta m)\alpha}} \approx \frac{\omega_0}{\Delta m} + \left(1 + \frac{2m}{\Delta m} \right) \alpha \omega_0.$$

For $\alpha \ll 1$, these are simply $\Delta\omega \approx \omega_0/\Delta m$, which is consistent with our experiment. The fringe separation does not depend on the spectral phase ϕ_n , although the time domain pulse shapes do.

There exist alloharmonics with $\Delta m = 1$ and fringe separation of approximately but not exactly ω_0 and spectral peaks *not* at harmonic positions $(n + \delta n)\omega_0$. In the quadratic phase case, they appear at frequencies

$$(7) \quad \omega_{A1} \approx \frac{\omega_0 |\Delta n|}{2|\alpha|}$$

(Fig. 2c4 at $\omega_{A1} \approx 165\omega_0$ and dotted lines in Fig. 2e). Observations of these $\Delta m = 1$ alloharmonics might easily be misinterpreted as harmonics.

More than two equalities in the alloharmonic equation (1) can hold simultaneously at approximately the same frequency: the spectrogram in Ext. Fig. 3a shows how three harmonic orders, $n = 54, 55$, and 56 , from pulses with numbers $m = -3, 0$, and $+3$ (thus, two pairs with $\Delta m = 3$ each), have nearly the same frequencies and therefore interfere producing fringes at $\omega \sim 55\omega_0$, with fringe spacing $\Delta\omega \approx \omega_0/3$. Indeed, the local portion of the spectrum around this frequency can be well represented by a sum of these three harmonics (Ext. Fig. 3b).

The alloharmonics are visible at relatively high frequencies, Eq. (5). The minimum frequency ω_{\min} at which alloharmonics are visible correspond to $|\Delta n| = 1$ in (5) and the maximum value of pulse number separation Δm_{\max} corresponding to sufficiently strong pulses. In our example of a Gaussian envelope with duration $\tau = 3T_0$ (three periods), fringes with separations down to $\Delta\omega_{\min} = \omega_0/6$ are visible at $\omega_{\min} \sim 28\omega_0$ (Fig. 2c2). Thus, the alloharmonics can be detected at minimum orders n_{\min} and frequencies ω_{\min} determined by the solution of (1) for $m = -\tau/T_0$, $\Delta m_{\max} = 2\tau/T_0$, and $\Delta n = -1$ for increasing and $\Delta n = +1$ for decreasing frequency. At frequencies lower than ω_{\min} , the harmonics can be considered "normal", although the transition is gradual. On the other hand, starting from some higher frequency ω^* ,

corresponding to interference between even stronger pulses with separation $\Delta m^* = \tau/T_0$, ($\Delta m^* = 3$ in our example), the alloharmonic fringes with separations of $\Delta\omega = \omega_0/\Delta m^*$ become the dominant spectral feature (Fig. 2c3, $\Delta\omega^* = \omega_0/3$ at $\omega^* \sim 56\omega_0$). For the quadratic phase,

$$(8) \quad n_{\min} \approx \frac{\omega_{\min}}{\omega_0} \approx \left| \frac{T_0}{4\alpha\tau} \right| = \left| \frac{\pi}{2\alpha\omega_0\tau} \right|,$$

$$n^* \approx \frac{\omega^*}{\omega_0} \approx \left| \frac{T_0}{2\alpha\tau} \right| = \left| \frac{\pi}{\alpha\omega_0\tau} \right|.$$

As $|\alpha|$ increases, the alloharmonics shift towards lower frequencies. Fig. 2e and Supplemental Animation 1 show the spectrum variation with α . The estimates in (8) can also be used for non-Gaussian envelopes and higher-order phase cases with dominant quadratic term contributions.

The alloharmonic concept can be equivalently considered from another perspective. Due to the finite envelope duration and nonperiodicity, the spectrum of a single harmonic has a finite, increasing with the harmonic order, bandwidth. First, the higher-frequency part of the spectrum becomes considerably more sensitive to driver nonperiodicity, as seen in Fig. 2e and Ext. Fig. 3c, where the low-order harmonics are still narrow even at $\alpha = -0.01$, while higher-order harmonics are much wider. Second, this means that solutions of the alloharmonic equation (1) can be non-integer, i.e., the fringes can appear between the ideal harmonics. For a quadratic phase and Gaussian envelope, the width of single harmonic spectrum is

$\delta\omega_n = \frac{2}{\tau} \sqrt{1 + 4\pi^2\alpha^2(n + \delta n)^2 \frac{\tau^4}{T_0^4}}$ (Supplemental Note 1). At low orders, there are normal narrow-bandwidth nonoverlapping harmonics. At order n_{\min} , the widths of the individual harmonics become $\delta\omega_{n_{\min}} \approx 0.5\omega_0$, and the neighbouring harmonics start to overlap, producing alloharmonic fringes in the minima between the normal harmonics. At order n^* , $\delta\omega_{n^*} \approx \omega_0$, the neighbouring harmonics overlap completely, rendering normal harmonics invisible and alloharmonics dominant. For different envelope shapes, the situation is similar, although the details may differ; for example, for a flat-top temporal envelope, alloharmonics start to appear on top of the harmonic peaks.

Importantly, the chirp rate α and overall duration τ appear as products in the denominators in (8). First, this means that even for slightly inexact periodicity, there are still frequencies at which the alloharmonics become dominant. In our example, the relative frequency change during the entire pulse $\sim 2\alpha\tau/T_0$ is less than 2%, but the alloharmonics became dominant at $\omega^* \sim 56\omega_0$. Second, in frequency comb spectroscopy and pulsar studies, the envelope duration equals the observation time, which can be very long – up to tens of minutes or even hours. Thus, alloharmonics can appear even with extremely slow frequency changes. Third, for long pulses with $\tau \gg T_0$, Δm_{\max} is very large, leading to very closely spaced fringes. To observe these fringes, the resolving power, defined as $R = \frac{\omega_A}{\Delta\omega}$, must be much higher than that required to observe normal harmonics. For the quadratic phase, $R = \frac{\Delta n \sqrt{1 - 16\alpha^2(\tau/T_0)^2}}{2|\alpha|} \approx \frac{\Delta n}{2|\alpha|}$; in the lowest-order approximation, the resolving power does not depend on the selected spectral range because the fringe period in this approximation depends linearly on the frequency as $\Delta\omega \approx \frac{2|\alpha|}{\Delta n} \omega$. In our example, the minimum resolving power is $R_{\min} \approx 167$ for $\Delta n = 1$.

Cubic phase, $\Phi(t) = \omega_0 t \left(1 + \beta \left(\frac{t}{T_0} \right)^2 \right)$, arises, e.g., in a frequency comb originating from a cavity with accelerating mirror. Cubic phase produces alloharmonic fringes exhibiting two periods, with

separations approximately but not exactly $\Delta\omega \approx \omega_0$ between stronger and $\Delta\omega \approx \omega_0/\Delta m$ between weaker spectral peaks, Ext. Fig. 4a. For a cubic phase, the alioharmonic frequencies are $\frac{\omega_A}{\omega_0} \approx -\frac{1}{3\beta} \frac{\Delta n}{\Delta m^2} - \frac{5}{3} \Delta n$, the fringe separations are $\frac{\Delta\omega}{\omega_0} \approx \frac{1}{\Delta m} + \beta\Delta m$, and the required resolving power is $R \approx -\frac{\Delta n}{3\beta\Delta m}$. In contrast to the quadratic phase, the required resolving power for the cubic phase decreases with Δm and thus with the envelope duration or observation time. The frequencies at which alioharmonics appear and become dominant are $\frac{\omega_{\min}}{\omega_0} \approx \frac{1}{12|\beta|} \left(\frac{T_0}{\tau}\right)^2$ and $\frac{\omega^*}{\omega_0} \approx \frac{1}{3|\beta|} \left(\frac{T_0}{\tau}\right)^2$, respectively (Ext. Fig. 4b).

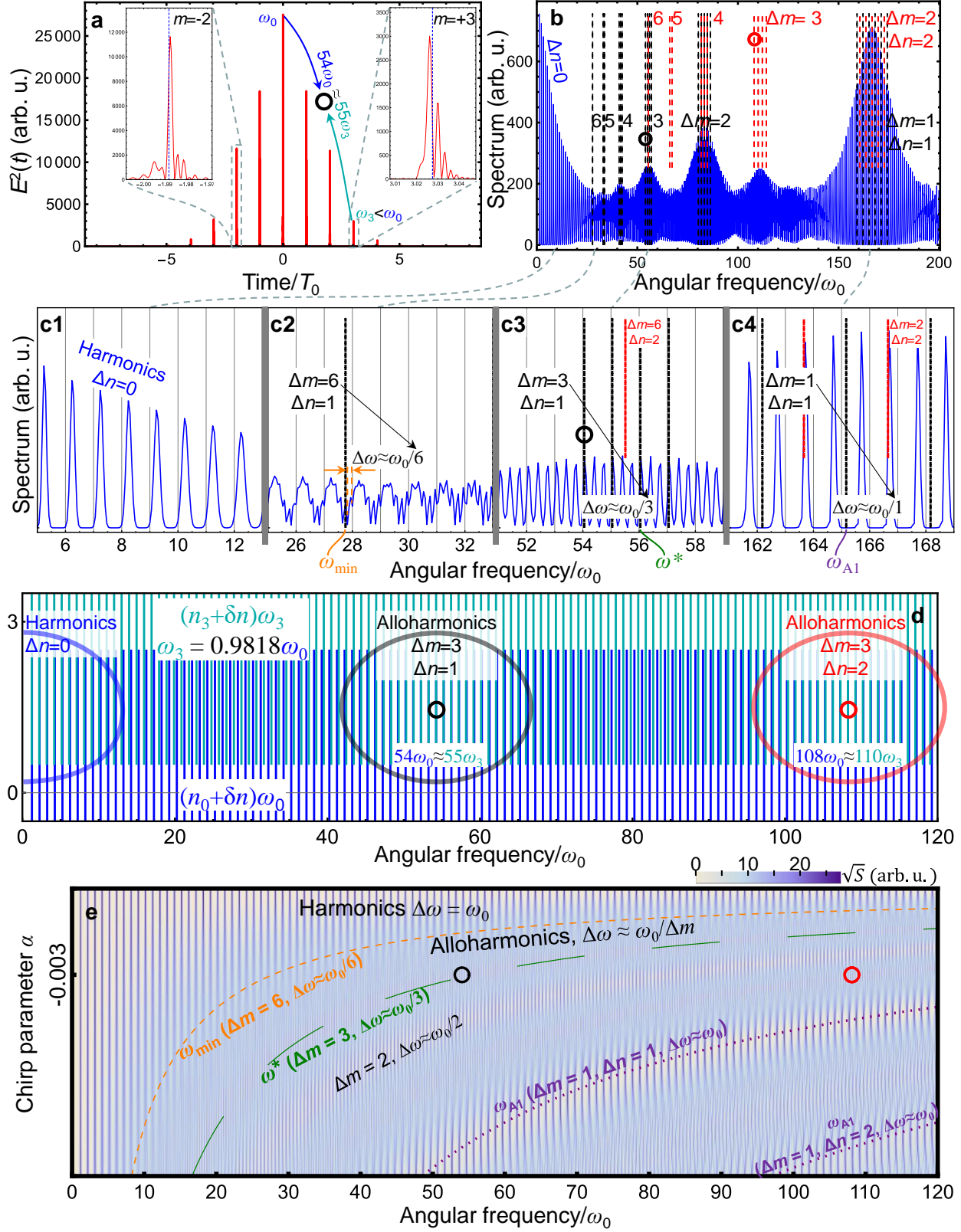


Fig. 2. **Alloharmonic generation by an almost periodic driver with quadratic phase with model parameters $\alpha = -0.003, \beta = \gamma = \delta = \dots = 0, \delta n = 0.25, n_{\max} = 200, a_n = 1, \phi_n = -[(n - 100)/75]^2$, and Gaussian envelope $A_\tau(t) = e^{-\frac{t^2}{\tau^2}, \tau = 3T_0$, Eqs. (2), (4). **a**, $E^2(t)$** ; the arrows indicate an example of interharmonic interference, Eq. (1), with $n = 54, \Delta n = 1, m = 0, \Delta m = 3$, i.e. interference of the 54th harmonic of the central pulse ($m = 0, \omega = \omega_0$) with the 55th harmonic of the pulse number $m = 3$ with lower frequency $\omega_3 < \omega_0$. This particular interference, which is a part of the alloharmonic series shown in Ext. Fig. 3**a, b**, is indicated by the small black circles in panels **a, b, c3, d, e**, Ext. Fig. 3**e**, and Supplemental Animation 1. Another interference example, $n = 108, \Delta n = 2, m = 0, \Delta m = 3$, is indicated by small red circles. The insets show individual pulses in the time domain corresponding to pulse numbers $m = -2$ and $m = +3$, and the vertical dashed lines indicate the calculated pulse positions (solutions of Eq. (3)). In a perfectly periodic case, these pulses occur at $t = -2T_0$ and $t = 3T_0$. **b**, Overall spectrum. Long black and short red vertical dashed lines in **b** and **c1-4** correspond to the $\Delta n = 1$ and $\Delta n = 2$ alloharmonics (solutions of Eq. (1)), with the Δm shown by the black ($\Delta n = 1$) and red ($\Delta n = 2$) numbers. **c1-4**, Spectra in limited bandwidth ranges: **c1**, normal harmonics, $\Delta n = 0$, with fringe separations of $\Delta\omega = \omega_0$, **c2-4**, alloharmonics with the main fringe separations of $\Delta\omega \approx \omega_0/6$ ($\Delta m = 6, \Delta n = 1$) in **c2**, $\Delta\omega \approx \omega_0/3$ (mainly $\Delta m = 3, \Delta n = 1$) in **c3**, and $\Delta\omega \approx \omega_0/1$ (mainly $\Delta m = 1, \Delta n = 1$) in **c4**; the calculated interharmonic interferences are indicated by the vertical dashed lines. **d**, Moiré pattern of the harmonic combs of the $m = 0$ (blue) and $m = 3$ (cyan) pulses (arrows in **a**). The large ellipses show three interference regions corresponding to harmonics with normal interference of the same harmonic orders, $\Delta n = 0$, and alloharmonic interferences with interharmonic separations $\Delta n = 1$ and $\Delta n = 2$. **e**, Variation in the spectral amplitude with the chirp parameter α (also shown in Supplemental Animation 1). The dashed orange line, ω_{\min} in Eq. (8), separates regions of harmonics and alloharmonics; alloharmonics are a dominant spectral feature on the right from the long-dashed green line, ω^* in Eq. (8). Dotted lines show frequencies $\omega_{A1}(\Delta m = 1, \Delta n = 1)$ and $\omega_{A1}(\Delta m = 1, \Delta n = 2)$, Eq. (7), where the alloharmonic fringe separation $\Delta\omega \approx \omega_0/\Delta m$ is approximately ω_0 .

Alloharmonics in experiments on coherent extreme ultraviolet generation via the BISER mechanism.

We now see that all the confusing properties of the experimental spectrum in Fig. 1, i.e., different fringe periods with approximately rational ratios: ≈ 1 and $\approx \frac{1}{2}$ in this case, and presence of nodes or antinodes at integer multiples of apparent fringe period, all correspond to alloharmonics. With the alloharmonic theory, we can explain the entire complex experimental spectrum and gain insights into driver properties.

We fit the experimental spectrum with the alloharmonics model with a fixed zero carrier-envelope offset and spectral phase ($\delta n = 0, \phi_n = 0$) (Fig. 3**a** red line, Ext. Fig. 5**a**). We stress that a small number of alloharmonic parameters can be used to precisely describe the complex experimental fringes. In contrast, a harmonic model with a constant frequency did not fit the data well (Ext. Fig. 5**b**); the Bayesian information criterion (BIC) decisively favours the alloharmonic model, with a ΔBIC of approximately 600.

The fit gave $\hbar\omega_0 = 0.63123 \pm 0.00010$ eV ($\lambda_0 = 1964.2 \pm 0.3$ nm), which is ~ 2.4 times lower than the laser frequency. We checked that frequencies close to the laser frequency ($\hbar\omega_L \approx 1.53$ eV) gave a poorer fit with $\Delta\text{BIC} > 1000$. This sensitivity to frequency leads to precise parameters determination and small fitting errors.

The fitted dimensionless chirp parameters were relatively large, with the leading term being $\alpha = -(1.684 \pm 0.007) \times 10^{-2}$. The positions of the five strongest pulses in the time domain (solutions of (3)) were significantly shifted from those of the periodic case and were larger than $0.1T_0$ for $m = \pm 2$, which is consistent with notable deviation in the fringe periodicity from $\hbar\omega_0/2$ (Fig. 1b2). The residuals, i.e., the pulse shifts compared to a periodic case, $\Delta t_m/T_0 = t_m/T_0 - m$, and pulse amplitudes are shown in Fig. 3b. This experiment and fit demonstrate that the alloharmonic concept allows precisely determining nonperiodic driver parameters, such as the central frequency and its time variation, even for high chirp orders, up to δ in our case.

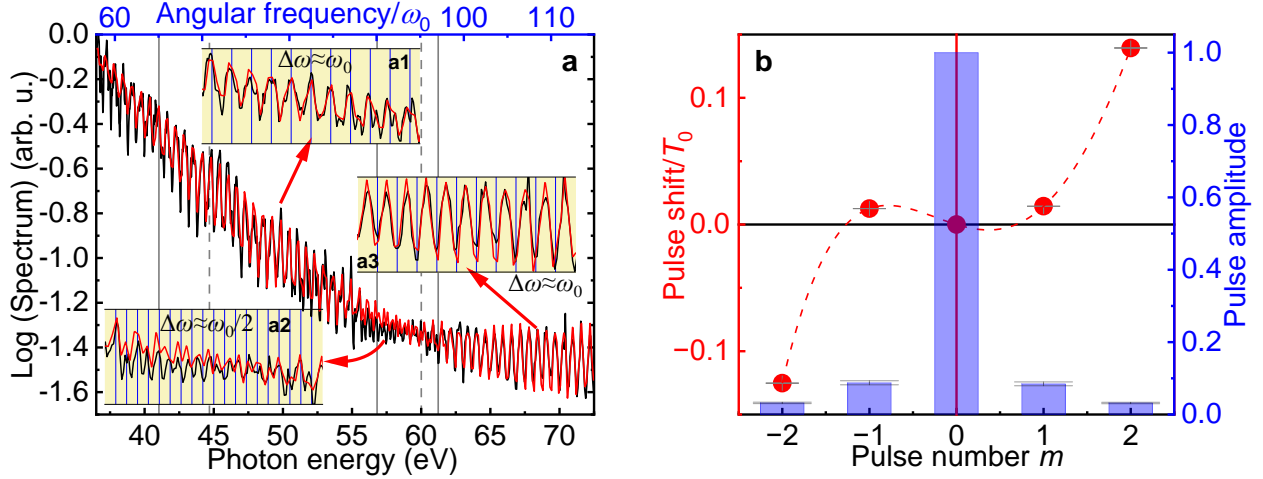


Fig. 3. **Alloharmonic fit of the experimental BISER spectrum.** **a**, Black, the experimental BISER spectrum (same as Fig. 1a black); red, the alloharmonic fit (Ext. Fig. 5a) with the fundamental photon energy $\hbar\omega_0 = 0.63123$ eV (wavelength $\lambda_0 = 1964.2$ nm) and other fit parameters shown in Ext. Fig. 5a. Grey vertical lines indicate the positions of alloharmonics with interharmonic separations Δn from 1 to 4 and separations of pulses in the time domain with $\Delta m = 1$ (solid lines) and $\Delta m = 2$ (dashed lines), which explain the spectral fringes with spacings of $\Delta\hbar\omega \approx \hbar\omega_0/\Delta m = \hbar\omega_0$ and $\approx \hbar\omega_0/2$, respectively. **b**, Five strongest time-domain pulses calculated from the alloharmonic model. Red circles (left axis) show the normalized shifts (residuals) from the periodic positions, $\Delta t_m/T_0 = t_m/T_0 - m$, where the period $T_0 \approx 6.55$ fs corresponds to the fundamental photon energy $\hbar\omega_0$. The error bars (some are difficult to see) are calculated by the error propagation technique from the fit standard errors.

Alloharmonics of gravitational waves emitted by binary black hole mergers

Binary black holes inspiral because they lose energy by emitting gravitational waves. As the distance between the two black holes gradually decreases, the orbital frequency increases. Thus, we expect to observe alloharmonics in the emitted gravitational wave spectra.

Direct measurements of the gravitational wave spectra of black holes are currently unavailable; thus, we used a gravitational waveform from state-of-the-art numerical relativity calculation published in the Simulating eXtreme Spacetimes (SXS) Collaboration catalogue^{14,15} (red line in Fig. 4a) describing a sufficiently long (more than 50 periods) evolution. The orbital frequency of this system increases slowly at first but quite rapidly near the merger at $t \sim 24\,000M$ (blue line in Fig. 4a; we use geometric units; here, M is the sum of gravitating masses). We assume that a gravitational spectrometer would have a millisecond-range Gaussian time window, such as two examples shown in Fig. 4a: for a combined binary

mass of $20M_{\odot}$ (20 solar masses), these window durations are ~ 100 ms. Results for other window durations are in Supplemental Note 2.

The high harmonics are well phased, evidenced by short gravitational wave bursts (Fig. 4b). These bursts are analogous to the attosecond pulses generated by laser harmonics²¹. The positions of these bursts are well described by Eq. (3), with the phase $\Phi(t)$ determined from integrating the orbital frequency dependence $\omega_{\text{Orb}}(t)$.

The spectra in the two windows are shown in Fig. 4c and d, and the spectrum evolution in the moving window in Supplemental Animation 2. Initially, the windowed spectrum consists of normal harmonics because the orbital frequency is approximately constant (Fig. 4c). However, as the inspiral progresses, the orbital frequency change accelerates, and within the same window duration, the frequency increases by more than 20% (Supplemental Note 2). In the second window, alloharmonics emerge starting at $4\omega_{\text{Orb}}$, corresponding to interharmonic separations $\Delta n = -1$, i.e., interferences with order n at time t_m and order $n - 1$ at time $t_{m+\Delta m} > t_m$ (Fig. 4d). These interferences (calculated with the alloharmonic equation (1)) are shown by the dashed vertical lines in Fig. 4d. The gravitational wave spectrum intensity decreases rapidly with increasing frequency; hence, larger interharmonic separations ($\Delta n = -2$, etc.) are less pronounced. A moderate resolving power of $R_{\text{min}} \approx 29$ would be required to observe these gravitational wave alloharmonics. The chirp rate in this example is orders of magnitude larger than that induced by the Earth's rotation and motion, and therefore, these alloharmonics can be observed without correction to the solar system's barycentre.

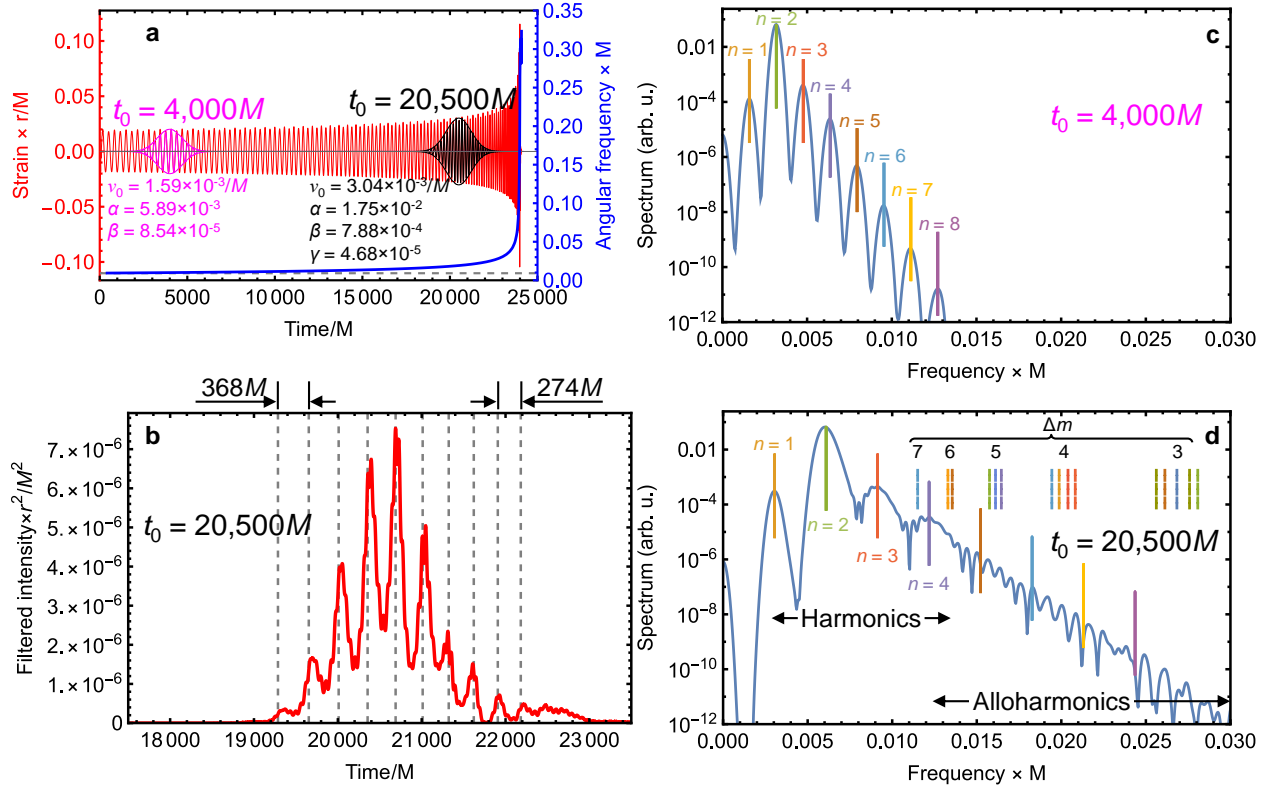


Fig. 4. **Alloharmonics in a gravitational wave emitted by an inspiralling binary black hole.** a, Red (left axis), normalized strain vs. time, numerical relativity calculation from the SXS Gravitational Waveform

Database¹⁵ SXS:BBH:1148, with a mass ratio of 2.038, dimensionless spins of 0.43 and 0.51, and initial orbital angular frequency of $\omega_{\text{orb,ini}} = 9.165 \times 10^{-3}/M$. Magenta and black colours indicate the windowed strains used in our calculations (Gaussian windows with indicated centres t_0 and durations $\tau = 1000M$) and the corresponding fitted frequency and chirp parameters. The blue line (right axis) represents the calculated instant orbital frequency; the horizontal grey dashed line shows the initial orbital frequency $\omega_{\text{orb,ini}}$. **b**, Short bursts of gravitational waves produced by a summation of harmonics with $n = 3$ and higher in the black window in **a**. Vertical dashed lines show the burst positions calculated by Eq. (3). **c, d** Spectra of strains in magenta and black windows in **a**, respectively; solid vertical lines show normal harmonics calculated from the orbital frequency shown in **a**. Dashed vertical lines show the alloharmonics, i.e. calculated positions (solutions of Eq. (1)) of the $\Delta n = -1$ interharmonic interference series, with Δm shown above. The number of alloharmonic fringes between the positions of normal harmonics is approximately equal to the corresponding Δm . In all frames, M is the sum of the two Christodoulou masses, i.e., gravitating masses including the rotational energies; the time unit is GM/c^3 , and the length unit of distance r is GM/c^2 (geometric units). For $M = M_{\odot}$ (one solar mass), these are $4.93 \mu\text{s}$ and 1.48 km , respectively.

Alloharmonics in frequency combs

Optical frequency combs are spectra of highly periodic pulse trains generated by a laser pulse bouncing in a stabilized cavity with a partially transmissive output coupler. Frequency combs, which are composed of equally spaced spectral lines, revolutionized precision spectroscopy by enabling fast self-calibrated measurements with atomic clock accuracy^{5,6,16,17} and temporal coherence up to 2000 s (Ref.³⁹). Here, we consider an optical comb from a slightly nonperiodic pulse train, generated by an in-vacuum cavity whose end mirror moves with a velocity $V \ll c$, where c is the speed of light in vacuum; the optical path is $2(L_0 + Vt)$, where L_0 is the initial cavity length and $T_0 = 2L_0/c$ is the initial round-trip period. The m -th pulse in the train occurs at $t_m = \frac{L_0}{V} \left[\left(\frac{c+V}{c-V} \right)^m - 1 \right] \approx T_0 \left(m + \frac{V}{c} m^2 + \dots \right)$, yielding the chirp parameter $\alpha = -V/c$ (Supplemental Note 3). Due to the Doppler shift, the alloharmonic equation (1) reads $(n + \delta n) \left(\frac{c-V}{c+V} \right)^m \omega_0 = (n + \delta n + \Delta n) \left(\frac{c-V}{c+V} \right)^{m+\Delta m} \omega_0$, yielding $n = \frac{\Delta n}{\left(\frac{c+V}{c-V} \right)^{\Delta m} - 1} - \delta n$. For $V \ll c$, the minimum order corresponding to alloharmonics with $\Delta n = 1$ is $n_{\min} \approx \frac{c}{2\Delta m|V|} = \frac{1}{2\Delta m|\alpha|}$, and the required resolving power is $R_{\min} \approx \frac{c}{2|V|} = \frac{1}{2|\alpha|}$. For a typical $L_0 = 150 \text{ cm}$ cavity length (round-trip time $T_0 \approx 10 \text{ ns}$, repetition rate $\nu_0 \approx 100 \text{ MHz}$), velocity $V = 1 \text{ mm/s}$, and observation time $\tau = 1 \text{ ms}$ ($\Delta m \approx 10^5$ pulses and a total mirror shift of $1 \mu\text{m}$), these yield $\alpha \approx -3.34 \times 10^{-12}$, and alloharmonics replace the normal comb at $n > n_{\min} \approx 1.5 \times 10^6$, frequencies $\nu > 150 \text{ THz}$ and wavelengths $\lambda < 2 \mu\text{m}$, i.e., in the entire near-infrared, visible, and ultraviolet regions. The required resolving power in this case is $R_{\min} \approx 1.5 \times 10^{11}$. Alloharmonics in frequency combs allow precise velocity measurement or stabilization and comb density control without changing the cavity. For precision frequency metrology, denser combs provide a larger number of reference frequency points at more localized positions in the spectrum, facilitating higher accuracy; on the other hand, this requires higher resolving power and thus often need to be avoided; for the latter cases, alloharmonics determine the maximum cavity stabilization velocity.

Further, alloharmonics in optical frequency combs allow precise measurements of extremely small accelerations. This provides a new method for testing gravity theories such as modified Newtonian dynamics⁴⁰, which requires sensitivity to accelerations of $a \sim 10^{-10} \text{ m/s}^2$. An accelerating cavity mirror induces a cubic phase with $\beta = -aT_0/3c$, and thus, alloharmonics can be observed at frequencies $\nu > \frac{\nu_0}{3|\beta|\Delta m^2} = \frac{c}{a\tau^2}$ with resolving power $R > \frac{1}{3|\beta|\Delta m} = \frac{c}{a\tau}$. For a $\tau = 100 \text{ s}$ observation time, these give $\nu > 300 \text{ THz}$ ($\lambda < 1 \mu\text{m}$) and $R \sim 3 \times 10^{16}$; a longer observation time reduces the required resolving power.

Alloharmonics in radio emission of pulsars

Pulsars are spinning neutron stars emitting periodic electromagnetic radiation, similar to a lighthouse⁴¹. Pulsar radio spectra are coherent, consisting of harmonics of the rotation frequency. Fourier transforms of the pulsar radiation intensity, i.e., their power spectra, contain interesting features⁴². The pulsar rotation decelerates gradually, thus providing conditions for generating alloharmonics. Some pulsars exhibit rare glitch events³⁷, which can be interpreted as a sudden increase in the rotation frequency, and can provide information about pulsar structure and physics.

A typical pulsar has an approximately constant rotation frequency ν_0 with a very small time derivative $\dot{\nu}$, producing the chirp parameter $\alpha \approx \dot{\nu}/2\nu_0^2$ (Supplemental Note 4). For an observation time window consisting of N_p periods, the alloharmonics can be observed at orders $n_{\min} = -\nu_0^2/N_p\dot{\nu}$ and the corresponding frequencies $\nu_{\min} = -\nu_0^3/N_p\dot{\nu}$. The required resolving power is $R_{\min} = -\nu_0^2/\dot{\nu}$, which does not depend on the observation time.

In our examples, which are described in Ext. Data Table 1 and Supplemental Note 4, we assume a $\sim 200 \text{ s}$ observation time, which is typical of meridian instruments⁴² rotating with the Earth; however, other instruments can have longer time windows. The Vela pulsar (J0835-4510, age $\sim 1.1 \times 10^4$ years) has $\nu_0 = 11.1946499395 \text{ Hz}$ and $\dot{\nu} = -1.5666 \times 10^{-11} \text{ Hz}^2$ (Ref.⁴³). These parameters yield $\alpha \approx -6.25 \times 10^{-14}$ and $N_p = 2300$ periods in a 205 s time window. Moreover, the minimum harmonic order above which alloharmonics appear is $n_{\min} \approx 3.48 \times 10^9$ at frequencies above $\nu_{\min} \approx 38.9 \text{ GHz}$, and the required resolving power $R_{\min} \approx 8.0 \times 10^{12}$. For the older Geminga pulsar⁴⁴, α is smaller, and the alloharmonic frequency is higher. For young pulsars, the deceleration is much faster; for example, for SGR 1806-20 (J1808-2024, age ~ 220 years), $\nu_0 = 0.1323466 \text{ Hz}$ and $\dot{\nu} = -9.62 \times 10^{-12} \text{ Hz}^2$ (Ref.⁴³), yielding $\alpha \approx -2.75 \times 10^{-10}$ and $N_p = 27$ periods in a 204 s time window, a harmonic order of $n_{\min} \approx 6.74 \times 10^7$, a frequency of $\nu_{\min} \approx 8.92 \text{ MHz}$, and a resolving power of $R_{\min} \approx 1.8 \times 10^9$. Alloharmonics from the same pulsar can be observed in a considerably shorter window, with $N_p = 2$ periods (~ 15 seconds, 3 pulses) and $n_{\min} \approx 9.10 \times 10^8$, $\nu_{\min} \approx 120 \text{ MHz}$, and the same resolving power. Thus, the spectra of young pulsars contain mostly alloharmonics within typical radio telescope bands, i.e., the atmosphere's radio window, $\sim 20 \text{ MHz}$ to 1 THz , while older pulsars have normal harmonics up to a few tens of GHz and alloharmonics at higher frequencies.

The chirp parameter for a glitch is $\alpha = \Delta\nu_G/4\pi N_G\nu_0$ (Supplemental Note 4), where $\Delta\nu_G$ and N_G are the frequency change and number of periods during the glitch. The minimum order and frequency above which alloharmonics can be observed are $n_{\min} = 2\pi\nu_0/\Delta\nu_G$ and $\nu_{\min} = 2\pi\nu_0^2/\Delta\nu_G$, and the required resolving power is $R_{\min} = 2\pi N_G\nu_0/\Delta\nu_G$ (Supplemental Note 4). For example, the 2016 Vela glitch had $\Delta\nu_G/\nu_0 = 1.431 \times 10^{-6}$ and a duration of $N_G = 49$ periods (4.4 seconds)³⁷. For this example, $\alpha =$

2.32×10^{-9} , the alloharmonics are present above $n_{\min} \approx 4.39 \times 10^6$ and $\nu_{\min} \approx 49.2$ MHz, and $R_{\min} \approx 2.2 \times 10^8$.

Importantly, a pulsar's apparent nonperiodicity is also caused by the Earth rotation and orbit: motion along a circle with radius r and angular frequency Ω induces the chirp coefficient $\alpha \approx -\frac{r\Omega^2}{2cv_0}$ for an in-plane propagating plane wave (Extended Data Table 1, Supplemental Note 4). Despite this, glitch alloharmonics can be observed, as glitches induce much larger chirp coefficients. Spin-down alloharmonics of the youngest pulsars can be observed by spaceborne instruments orbiting the Sun. For older pulsars, a correction to the solar system's barycentre, or a special case of wave propagation perpendicular to the rotation plane would be required.

Discussion

A reliable alloharmonic observation, as exemplified by our BISER experiment, must satisfy two conditions: First, sufficient resolving power to observe much-finer-than-harmonics alloharmonic fringes; Second, observation of at least two different fringe periods. The same conditions apply for reliable harmonics observations, to distinguish them from alloharmonics. These conditions are challenging, especially at very high harmonic orders^{45,46}. Whereas several high-quality experiments, such as⁹⁻¹¹, satisfied these conditions, we argue that alloharmonics can easily escape detection and cause significant errors. First, insufficient resolving power leads to absence of expected harmonic fringes, which can be misinterpreted as absence of temporal coherence or even as a single peak ("isolated attosecond pulse") in the time domain, whereas much finer alloharmonic fringes are present but remain unresolved. Second, a spectral fringe period and positions of the spectral components observed in a narrow bandwidth can be misinterpreted as a base frequency and carrier-envelope offset, whereas this is incorrect for alloharmonics; this misinterpretation is especially probable for alloharmonics with pulse separation $\Delta m = 1$, for which the spectral fringe period, $\Delta\omega \approx \omega_0/\Delta m$, is approximately (but not exactly) equal to the driver period, ω_0 .

We note that observation of alloharmonics in optical frequency combs and pulsar spectra require very high resolving powers which are not practical with standard spectrometers (as they would have light-minutes sizes), but can be obtained with dual-comb spectroscopy^{17,47}. Also, the analytical formulas (Supplemental Note 1) used to calculate interharmonic interference, Ext. Fig. 3b, can be used to calculate very-high-frequency spectra, for which numerical Fourier transform is impractical as it requires much computational time (Supplemental Note 4).

Alloharmonics from the BISER experiment, Ext. Fig. 5a, and black hole merger, Fig. 4a, have almost the same absolute values of dimensionless chirp α , although the signs are opposite. However, the alloharmonic spectrum is not sensitive to the time direction. Thus, if only the spectral shape and its fringes are important, this provides a basis for scaled, i.e., with the same dimensionless parameters, laboratory astrophysics experiments, where the gradually decreasing frequency in an experiment can be used to model both processes with decreasing and increasing frequencies.

Conclusion

Alloharmonic theory fills in a gap of knowledge related to the present laser-driven harmonic experiments. Furthermore, it predicts yet-to-be-observed alloharmonic spectra in optical frequency

combs and astrophysics. Like our rich experimental spectra, these observations will allow inferring the driver periodicity and nonperiodicity parameters. However, we expect that, somewhat counterintuitively, these spectra will be most interesting and informative by their dissimilarities with the "simple" alloharmonics due to such effects as higher chirp orders, possible reduction in the coherence degree and pulsar nullings³⁷, binary black hole inspiral in presence of other objects, and other yet-to-be-discovered factors which will require further research and expanded models.

Data availability

The data are available from the authors on reasonable request.

Code availability

The code written in the Wolfram Language is published in the Supplemental Notes.

Acknowledgements

We are grateful to the J-KAREN-P laser team and acknowledge discussions with V. M. Malofeev and S. B. Echmaev. This research was supported by JSPS Kakenhi JP26707031, JP19H00669 and JP19KK0355 and Strategic Grants by the QST President: Creative Research #20 and IRI.

Author contributions

ASP led the research, KO, AS, AYaF, TAP, HKo, YH, YF, HD, NH, MI, MN, MK, TK, HKi, MK, DN, and ASP prepared and performed the experiment, MSP proposed the alloharmonic explanation of the data, MSP, TZhE, JKK, SVB, and ASP developed the theory and applied it to BISER spectra, gravitational waves, frequency combs, and pulsar radio emission. MSP, TZhE, JKK, and ASP prepared the manuscript with contribution from other authors. All authors contributed ideas.

Competing interests

The authors declare no competing interests.

Methods

Experiment on coherent extreme ultraviolet generation via the BISER mechanism

Laser. We used a multi-terawatt femtosecond linearly polarized J-KAREN-P laser described previously⁴⁸ based on chirped pulse amplification technology⁷. The laser pulses had a central wavelength of $\lambda_L = 0.8115 \pm 0.0007 \mu\text{m}$, corresponding to the photon energy $\hbar\omega_L = 1.5278 \pm 0.0013 \text{ eV}$; here and throughout this paragraph, the errors listed are the standard deviation of the shot-to-shot parameter variations. The pulse energy was $\mathcal{E}_L = 0.648 \pm 0.011 \text{ J}$. The pulse duration and spot shape were measured in vacuum at full laser power attenuated with two wedges and additional high-quality neutral-density filters in the case of spot measurement. The pulse measured with self-referenced spectral interferometry⁴⁹ had a full width at half maximum (FWHM) duration of $33 \pm 5 \text{ fs}$ and an effective duration of $\tau_{\text{Eff}} = 38 \pm 6 \text{ fs}$. Here, $\tau_{\text{Eff}} = \int P_n(t)dt$ is the area under the normalized power curve $P_n(t)$ (Ref.⁵⁰). The peak power $P_L = \mathcal{E}_L/\tau_{\text{Eff}}$ was $17 \pm 3 \text{ TW}$. The pulses were focused with an $f/9$ off-axis parabolic mirror. The focal spot, measured with an achromatic lens and high dynamic range charge-coupled device

(CCD), had an FWHM of $(10.1 \pm 0.2) \mu\text{m} \times (12.1 \pm 0.5) \mu\text{m}$, horizontal (along the polarization direction) \times vertical, and an effective spot radius⁵⁰ of $r_{\text{Eff}} = 8.3 \pm 0.3 \mu\text{m}$. The estimated irradiance in the absence of plasma was $I_{L,\text{Vac}} = \frac{P_L}{\pi r_{\text{Eff}}^2} = (7.9 \pm 1.4) \times 10^{18} \text{W/cm}^2$, and the corresponding dimensionless amplitude was $a_{0,\text{Vac}} = 1.9 \pm 0.2$. In plasma, these values increased significantly due to relativistic self-focusing⁵¹⁻⁵³ (see below).

Gas jet. We used a 1-mm diameter supersonic helium gas jet with a Mach number of 3.3, as described previously⁵⁴. The peak electron density in the helium jet, which is controlled by the backing pressure, was set to $n_e \approx (2.6 \pm 0.8) \times 10^{19} \text{cm}^{-3}$. Here, the 30% error is due to interferometry reconstruction errors.

Relativistic plasma. In relativistic plasma, the electron velocity is close to the speed of light in vacuum, c . The electron dynamics in the laser field E_L are relativistic when the laser dimensionless amplitude, $a_0 = eE_L/m_e c \omega_L = (I_L/I_R)^{1/2}$, is comparable to or greater than unity⁵⁵. A laser is relativistically strong when $a_0 \geq 1$, as in our experiment. Here, e is the elementary charge, m_e is the electron mass, I_L is the peak irradiance, and $I_R = \pi m_e^2 c^5 / 2e^2 \lambda_L^2 \approx 1.37 \times 10^{18} \text{W/cm}^2 \times (\lambda_L [\mu\text{m}])^{-2}$ for a linearly polarized laser with angular frequency ω_L and wavelength λ_L . $\lambda_L [\mu\text{m}]$ denotes the laser wavelength in micrometres. For $\lambda_L = 0.81 \mu\text{m}$, we have $I_R \approx 2 \times 10^{18} \text{W/cm}^2$.

Laser propagation in relativistic plasma. In our case, the plasma was underdense (in the small amplitude limit⁵⁶); thus, its electron density $n_e \approx 2.6 \times 10^{19} \text{cm}^{-3}$ was much smaller than the critical density, $n_{\text{cr}} = \frac{m_e \omega_L^2}{4\pi e^2} \approx 1.1 \times 10^{21} \text{cm}^{-3} / (\lambda_L [\mu\text{m}])^2 \approx 1.7 \times 10^{21} \text{cm}^{-3}$. Thus, the laser pulse propagated through the plasma. Furthermore, the peak power $P_L = 17 \pm 3 \text{TW}$ significantly exceeded the threshold $P_{\text{SF}} = P_c \left(\frac{n_{\text{cr}}}{n_e} \right) \approx 0.6 \text{TW}$; thus, the laser underwent relativistic self-focusing⁵¹⁻⁵³. Here, $P_c = \frac{2m_e^2 c^5}{e^2} \approx 0.017 \text{TW}$, as described in Ref.⁵³. In the stationary self-focusing regime⁵⁷, the self-focused spot diameter and dimensionless amplitude are $d_{\text{SF}} = \lambda_L (a_0 n_{\text{cr}} / n_e)^{1/2} / \pi$ and $a_{\text{SF}} = (8\pi P_L n_e / P_c n_{\text{cr}})^{1/3}$, respectively. In our case, the estimated dimensionless amplitude after self-focusing was $a_{\text{SF}} \approx 7$.

A relativistically strong laser pulse propagating in underdense plasma excites wake waves such as longitudinal Langmuir waves⁵⁸. Moreover, when the focal spot is narrower than the threshold $d_{\text{BW}} = 2\lambda_L (a_0 n_{\text{cr}} / n_e)^{1/2} / \pi$, bow waves are generated⁵⁹⁻⁶¹. After relativistic self-focusing, this condition is always satisfied, as $d_{\text{SF}} < d_{\text{BW}}$, thus enabling excitation of prominent bow waves.

BISER mechanism. A relativistic irradiance laser pulse (peak irradiance $I_0 > 10^{18} \text{W/cm}^2$, $a_0 \geq 1$) propagating in underdense plasma (typical electron density $n_e \sim 10^{19} \text{cm}^{-3}$) generates plasma waves, significantly distorting the electron phase space and producing relativistic multistream plasma flow. In particular, phase space distortions corresponding to plasma waves such as wake waves^{58,62} and bow waves⁵⁹⁻⁶¹ can be observed. In terms of catastrophe theory^{63,64}, these distortions correspond to fold singularities and thus form sharp, high-density surfaces at the plasma cavity wall and bow wave front. At the joining of these two surfaces, a circular line of higher-order cusp singularity characterized by even higher density and sharpness forms. For a linearly polarized laser, this circular line divides into two sharp high-density crescents. The electrons driven by the strong laser and plasma fields emit high-frequency radiation, which adds coherently within these singularity regions due to their high density and sharpness. For high frequencies, the coherence regions are small; thus, the BISER radiation is emitted from point-like

(nanoscale) sources¹³. Catastrophe theory establishes that (i) the presence of multistream flows guarantees the formation of singularities, and (ii) the folds and cusps are structurally stable singularities, i.e., they do not disappear even under strong perturbations. Higher-order singularities may also form; however, they are not structurally stable. The BISER source generates extremely bright spatially and temporally coherent attosecond pulses that scale with the laser power; thus, the BISER source is considered a promising temporally and spatially coherent attosecond X-ray source^{12,13,54,65}.

BISER spectrum measurement. We used a grazing-incidence flat-field spectrograph⁵⁴ placed behind the gas jet (in the laser propagation direction). The spectrograph was composed of a gold-coated toroidal collecting mirror, a 200 μm slit, two 0.2 μm Al optical blocking filters, a spherical gold-coated varied line space (VLS) grating with a central line density of 1200 lines/mm, and a back-illuminated CCD. A 0.4 T, 5 cm-long magnet deflected charged particles away from the spectrograph. In contrast to previous experiments^{12,54}, the spectrograph covered a longer wavelength region of 17 – 34 nm, which was determined by the $L_{2,3}$ absorption edge of the Al filters at 17 nm and its second spectral order at 34 nm. In this spectral region, the achievable resolving power was much higher than that in previous experiments, which allowed observation of alloharmonics with considerably finer fringes than normal harmonics. The operating bandwidth was wide enough to observe alloharmonics with several Δm values, e.g., $\Delta m = 1, 2$ and 3 for the parameters in Fig. 1.

The spectrograph was carefully calibrated *in place* using the spectral lines of hydrogen-like helium and the position of the aluminium $L_{2,3}$ absorption edge, Ext. Fig. 1a, b and Ext. Fig. 2a. The true wavelengths of the He lines, namely, the ordinates shown in Ext. Fig. 2b, were taken from the NIST Atomic Spectra Database⁶⁶, and the Al absorption edge was determined from the X-Ray Interactions With Matter database^{67,68}. Each spectral line in the recorded helium spectrum was fitted with a Gaussian profile, and its centre was used as the corresponding abscissa. Thus, the line positions had subpixel accuracy. The dependence was fitted with a 3rd-order polynomial using OriginLab's OriginPro software⁶⁹ with the default settings (Ext. Fig. 2b), which provided an estimated accuracy of a few to several picometers (Ext. Fig. 2c).

The resolving power of the spectrograph was estimated from the BISER spectra using the finest observed fringes (red circles in Ext. Fig. 2d). At wavelengths shorter than 21 nm, the resolving power was limited by the pixel size, while at longer wavelengths, the resolving power was limited either by geometric aberrations or by the finest fringe spacing in the experiment. The resolving power was much higher than that required to observe normal harmonics of the initial laser frequency (black dashed line in Ext. Fig. 2d), and two times higher than that required to observe alloharmonics (Fig. 1), including alloharmonics with the redshifted frequency $\lambda_0 = 1964$ nm and Δm up to 3 (green dashed line in Ext. Fig. 2d).

The raw spectra contained contributions from both the BISER source and the He plasma (Ext. Fig. 1a), but the high reproducibility allowed the He contribution to be subtracted (Ext. Fig. 1c). These BISER-only spectra were used in the analysis.

Fitting of the experimental BISER spectrum with the alloharmonic model. We used the Simplex and Levenberg Marquardt algorithms in OriginPro software⁶⁹ (version 2022b build 9.9.5.167) to fit the experimental BISER spectrum with the alloharmonics.

First, we used the alloharmonic model, Eqs. (2) and (4), with a Lorentz-like envelope and zero carrier-envelope offset and spectral phase:

$$(9) E(t) = \left(1 + \frac{t^2}{\tau^2}\right)^{-\frac{2}{3}} \sum_n a_n \cos[n\Phi(t)].$$

The summation was performed from the 30th to 250th harmonics. The spectral amplitudes were represented as the double-exponent function $a_n = A_1 \exp(B_1 n \hbar \omega_0) + A_2 \exp(B_2 n \hbar \omega_0)$ to account for the overall spectral shape. The phase contained the chirp coefficients α, β, γ , and δ (Eq. (4)), as lower-order phases did not provide good fits to the data. Thus, there were 10 fit parameters: $\tau, A_{1,2}, B_{1,2}, \lambda_0, \alpha, \beta, \gamma$, and δ . Five parameters, $\tau, A_{1,2}$, and $B_{1,2}$, fit the overall spectrum shape and modulation depth and are not alloharmonic-specific. The remaining five parameters, $\lambda_0, \alpha, \beta, \gamma$, and δ , determined the alloharmonic properties. The resulting fitting curve and parameters are shown in Fig. 3a and Ext. Fig. 5a.

The dependence of the pulse position shift $t_m - mT_0$ on pulse number m , had a linear tilt with a slope $\approx 0.05\omega_0$ (Fig. 3b). This might be interpreted as a necessity to change the central frequency by this amount. However, this interpretation is incorrect, as most of the energy was concentrated at the pulses with $m = 0, \pm 1$, and thus, the three central pulses were the most important for the central frequency determination. The line passing through the three central points in Fig. 3b is approximately horizontal, confirming the correct value of the central frequency inferred from the fit.

To check that the central frequency cannot be selected close to the initial laser frequency, we performed a separate fit with the same model, but the central wavelength bounded to [750,1100] nm corresponding to photon energies of [1.13,1.65] eV. It gave a poor fit. We compared this fit with the previous one using the Bayesian information criterion (BIC), which is suitable because the number of data points (844 in our case) was much larger than the number of parameters; the Bayesian information criterion has an advantage as it requires no priors. The comparison showed that the original ($\lambda_0 = 1964.2 \pm 0.3$ nm, $\hbar\omega_0 = 0.63123 \pm 0.00010$ eV) alloharmonic model fit was decisively better, with $\Delta\text{BIC} = 1015$.

We also attempted to fit the experimental data with the normal harmonics, i.e., with a linear phase with $\alpha = \beta = \gamma = \delta = 0$, shown in Ext. Fig. 5c. The Bayesian information criterion showed that the harmonic model did not fit the data well, and that the alloharmonic model obtained a decisively better fit, with $\Delta\text{BIC} = 592$.

We note that the model spectrum is not sensitive to the overall spectral phase and time direction – i.e., the spectrum does not change when an overall spectral phase is added or time is reversed. Thus, our fitting procedure does not provide the attosecond pulse duration or the sign of the frequency change. In our case, we selected the time direction so that the frequency decreases gradually because the fundamental frequency of the BISER radiation was ~ 2.4 times lower than the initial laser frequency, thus requiring a generally decreasing trend.

Numerical relativity calculation of gravitational waves emitted by binary black hole mergers

We used gravitational waveforms obtained by numerical relativity calculations from the Simulating eXtreme Spacetimes (SXS) Collaboration catalogue^{14,15}. Specifically, we used centre-of-mass-corrected, non-extrapolated spherical harmonic modes from the outermost extraction radius. We calculated the strain from these modes using expressions for the spin-weighted spherical harmonics from Ref.⁷⁰. We

selected an in-plane observation direction because it contains much stronger harmonics than other observation directions. Details are in Supplemental Note 2.

The harmonic and alloharmonic spectra shown in Fig. 4c, d were calculated as the Fourier transforms of the strain in time windows shown in Fig. 4a by magenta and black lines, respectively. To compare these numerically calculated spectra with the analytical alloharmonic model, we calculated the time-dependent orbital frequency, as shown by the blue line in Fig. 4a, using interpolated zero-crossings of the strain and calculating the orbital period as four times the separation between these zero-crossings. The coefficient of 4 is necessary because there are two crossings per period, and the main gravitational wave contribution is emitted at the second harmonic of the orbital frequency. We checked that another method based on the separations between the positive and negative peaks of the strain produced consistent results (Supplemental Note 2).

The dependence of the orbital frequency on time was used to determine the local central frequency ν_0 and chirp coefficients α, β for the slowly varying frequency in the magenta time window in Fig. 4a, and α, β, γ for the faster-varying frequency in the black time window in Fig. 4a. These local central frequencies were used to calculate the frequencies of the normal harmonics $n\nu_0$ shown by the solid vertical lines in Fig. 4c, d, for which the 2nd harmonic dominates. The chirp coefficients were used to calculate the frequencies of the alloharmonic series using Eq. (1), shown by dashed vertical lines in Fig. 4d.

In Supplemental Animation 2, the orbital frequency gradually increases with time. Thus, the number of gravitational wave cycles in the constant-duration time window also increases. This differs from Supplemental Animation 1, where the number of wave cycles is constant. Therefore, in Supplemental Animation 2, when the alloharmonics first appear in the shown spectral band, they have a maximum $\Delta m = 4$, while as the inspiral progressed, this value increased up to $\Delta m = 8$. We set the animation frame rate to 8 frames per second (FPS), i.e., the animation frame duration of 125 ms. The physical frame duration in the animation is $100M$, thus, the 125 ms frame duration corresponds to $M \approx 250 M_\odot$. For $M \approx 25 M_\odot$, the animation would be ten times faster.

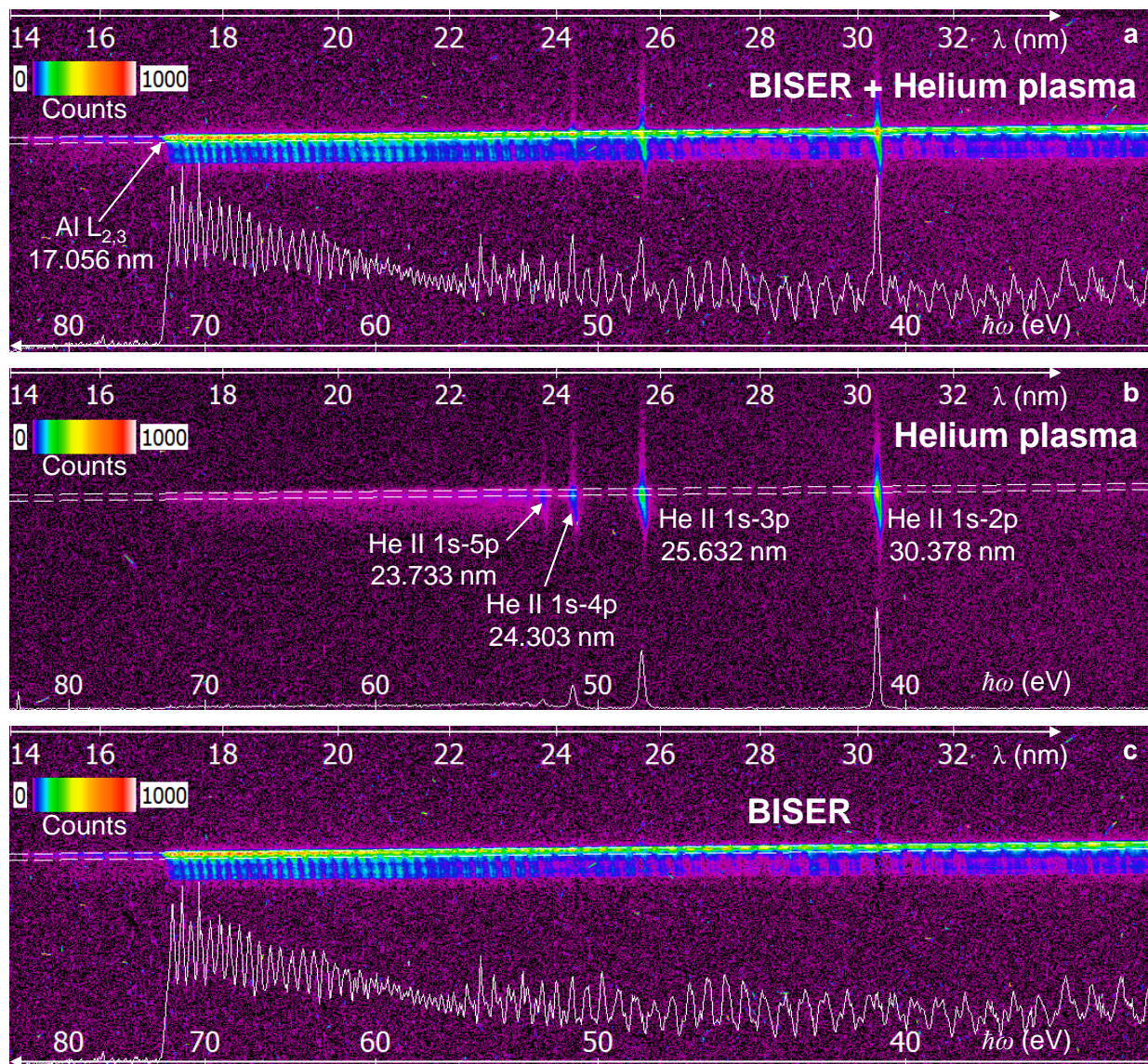
Alloharmonic spectrum for a Gaussian envelope and quadratic phase

For very high frequencies and harmonic orders, such as those in radio spectra of pulsars and in optical frequency combs, Fourier transforms can be very time-consuming. In the case of a Gaussian envelope and quadratic phase, the following analytical formula can be used (Supplemental Note 4):

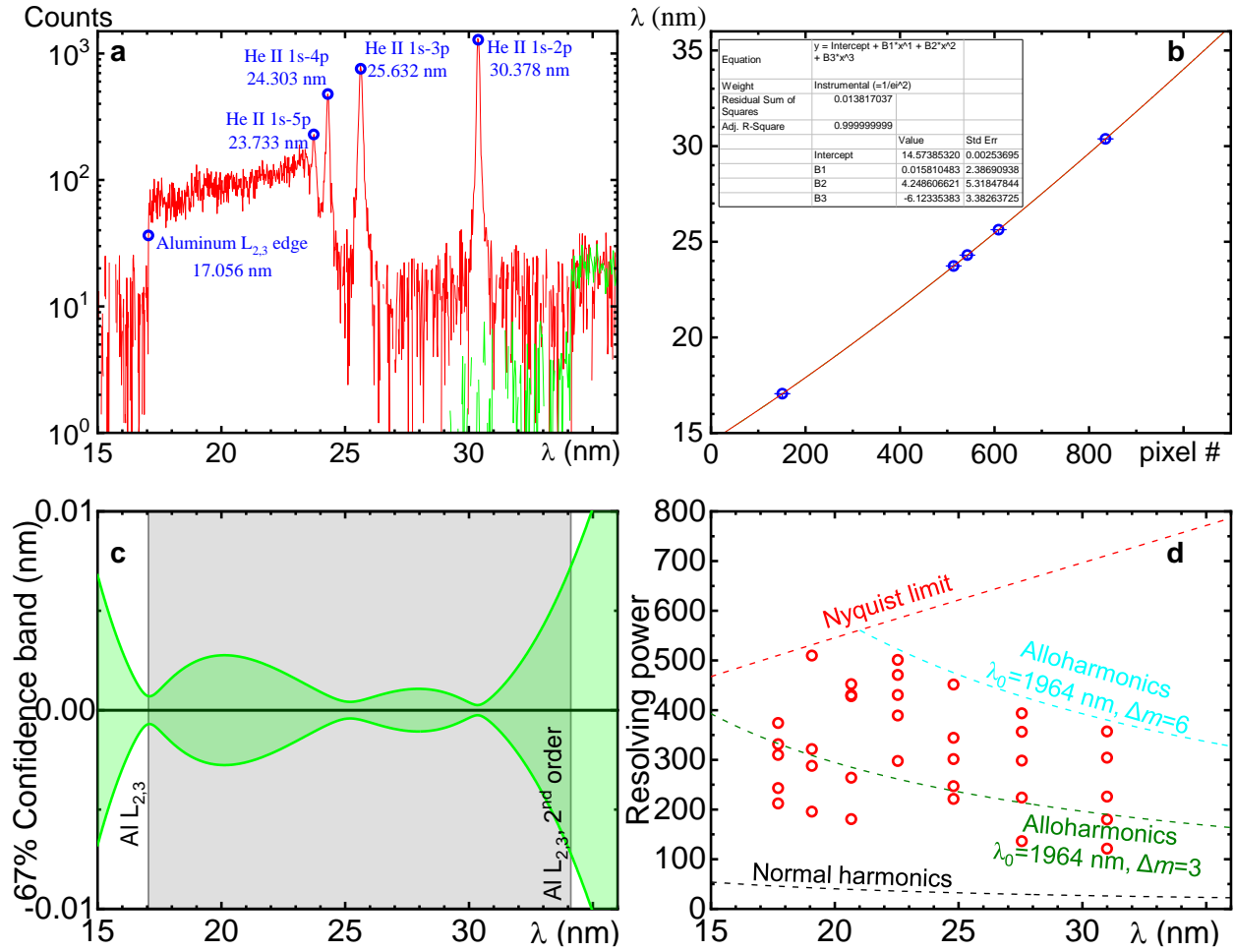
$$(10) E(\nu) = \sum_n \frac{a_n}{2\sqrt{2\left(\frac{T_0}{\tau}\right)^2 + i4\pi n\alpha}} \text{Exp}\left(-\frac{\left(\frac{\nu}{\nu_0} - n\right)^2 \pi^2}{\left(\frac{T_0}{\tau}\right)^2 + i2\pi n\alpha}\right),$$

The spectrum is then $S(\nu) = |E(\nu)|^2$. This formula was used to calculate interference of three and two harmonics, red and green lines in Ext. Fig. 3b, and model-based pulsar spectra in Supplemental Note 4.

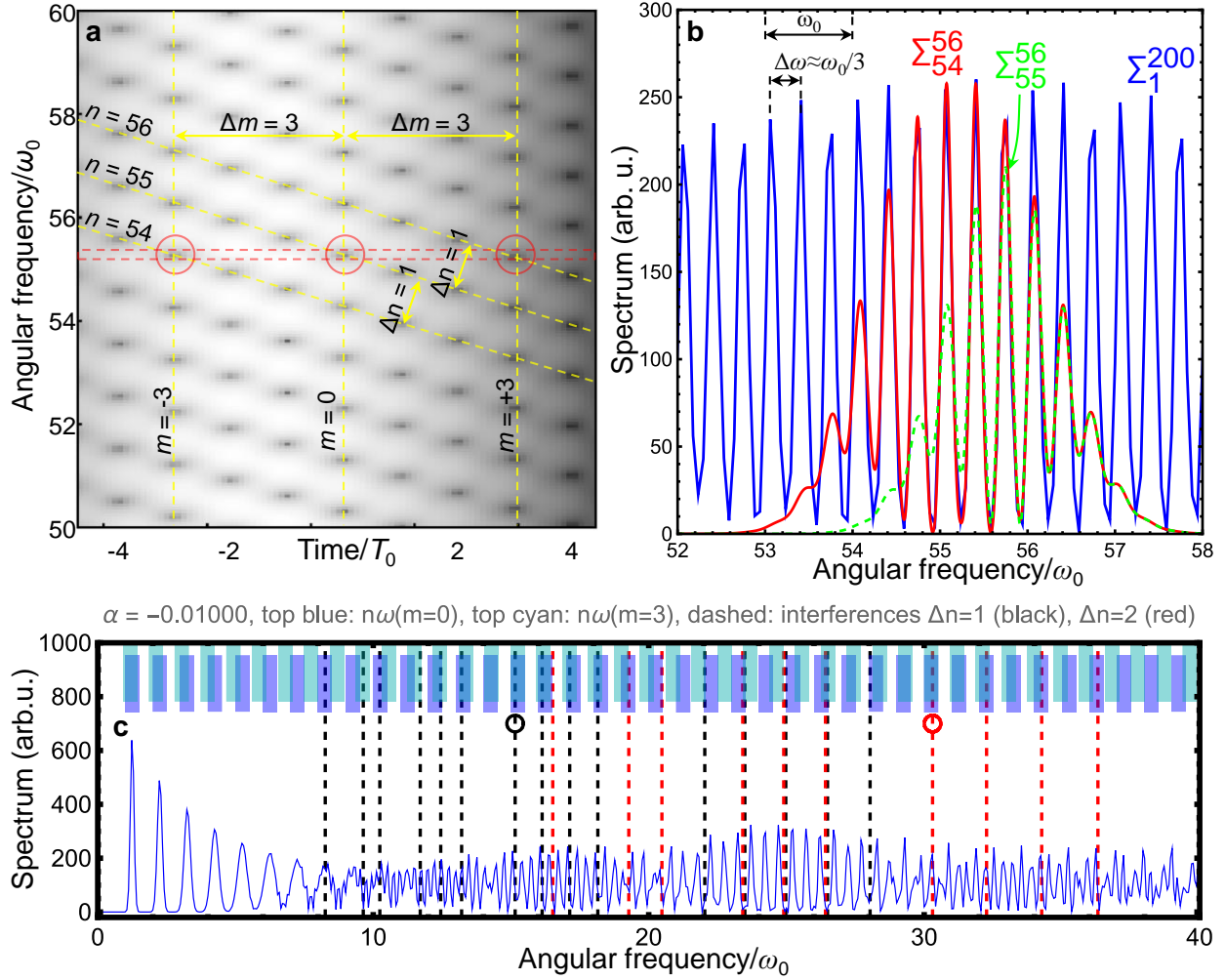
Extended Data Figures



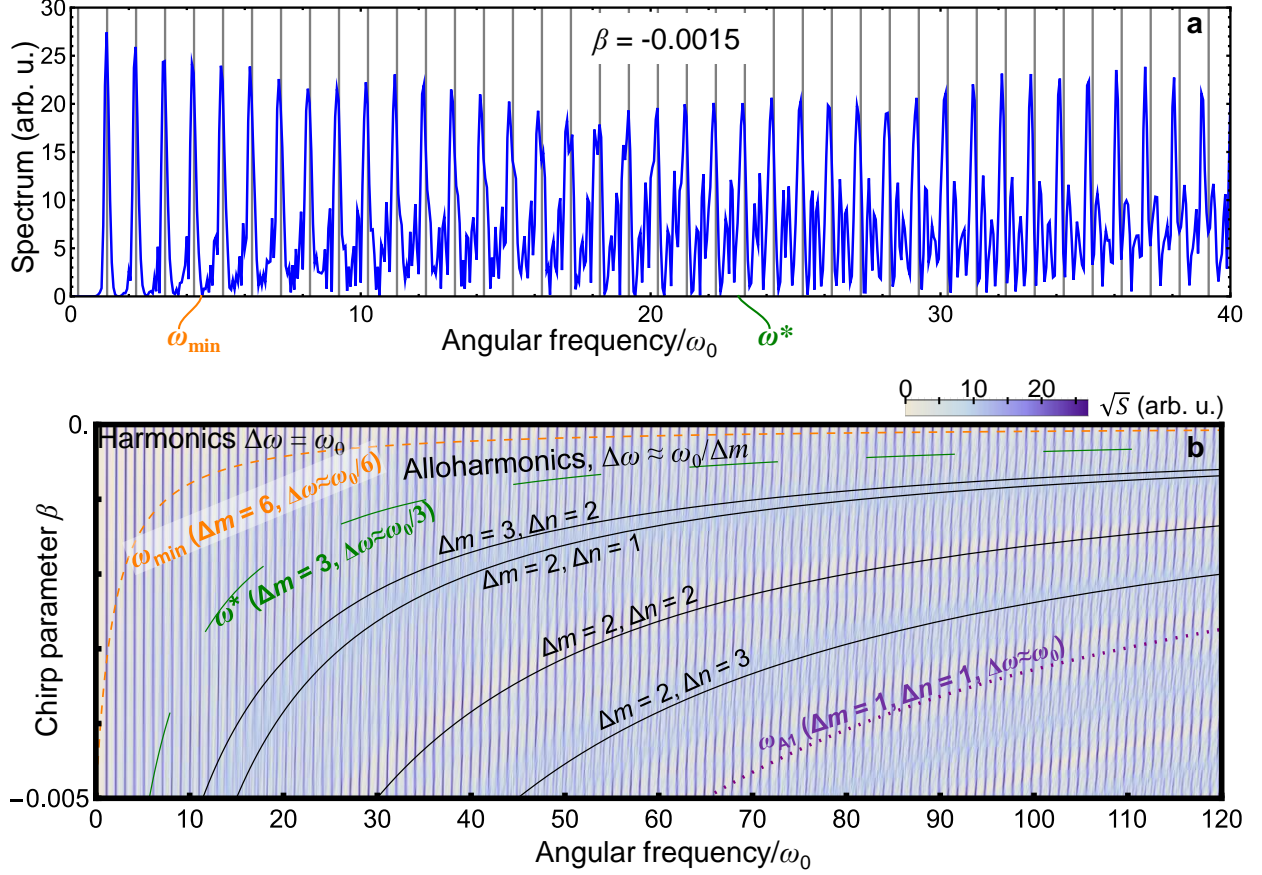
Ext. Fig. 1. **Raw data recorded by the spectrograph.** **a** Raw data with combined BISER and helium plasma spectra. **b** Helium plasma spectrum. **c** BISER spectrum obtained by subtracting **b** from **a**. Colour scales show charge-coupled device (CCD) counts; lineouts correspond to the dashed regions; the top and bottom axes correspond to the wavelength and photon energy, respectively.



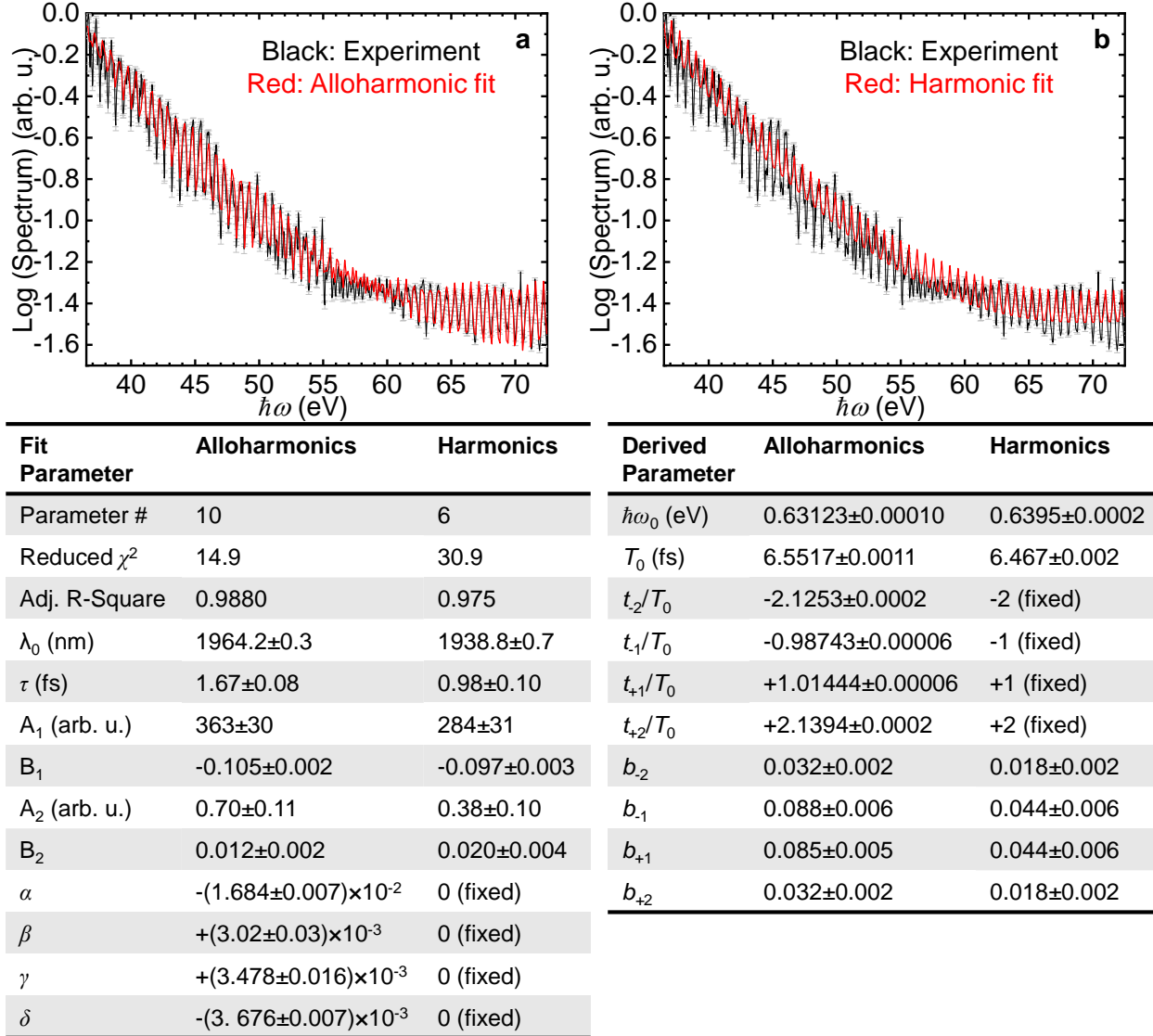
Ext. Fig. 2. **Spectrograph calibration and resolving power.** **a** Helium plasma spectrum excited *in place* by the same laser and recorded with the same spectrograph settings. Blue circles indicate spectral lines and the aluminium $L_{2,3}$ absorption edge used for wavelength calibration. **b** 3rd-order polynomial wavelength calibration (red line) through the He lines and aluminium $L_{2,3}$ absorption edge (blue circles, the error bars correspond to the standard errors). **c** Estimated 67% confidence band of the wavelength calibration fit; the grey shaded area shows the spectrograph operating band between the Al $L_{2,3}$ absorption edge and its second diffraction order. **d** Resolving power of the spectrograph estimated from fine BISER alloharmonic fringes observed under various conditions (red circles). The red dashed line denotes the resolving power limit corresponding to two CCD pixels, the lower black dashed line represents the resolving power required to resolve normal harmonics with initial laser wavelength $\lambda_0 = 0.81 \mu\text{m}$, and the green and cyan dashed lines represent the resolving powers required to resolve alloharmonics with red-shifted wavelength $\lambda_0 = 1.964 \mu\text{m}$ and $\Delta m = 3$ (as in Fig. 1) and $\Delta m = 6$, respectively.



Ext. Fig. 3. **Alloharmonic generation by a nonperiodic driver according to the model formulated in Eqs. (2), (4), with the quadratic phase with the same parameters as in Fig. 2. a**, Portion of a spectrogram. At the region of interest indicated by the red dashed lines at frequency $\omega \sim 55\omega_0$, there are three spectrogram peaks indicated by red circles. These spectrogram peaks correspond to different harmonics with orders $n = 54, 55, 56$ (tilted yellow dashed lines) from three different pulses with numbers $m = -3, 0, +3$ (vertical dashed yellow lines). **b**, Alloharmonics (interharmonic interference) corresponding to red circles in **a**: the spectrum (blue, sum of all harmonics) and its local approximation as a sum of three (red, orders $n = 54, 55, 56$) and two (dashed green, orders $n = 55, 56$) interfering harmonics with $\Delta m = 3$. **c**, Frame from Supplemental Animation 1 showing the variation in the spectrum as α changes from 0 to -0.01 (this frame). Blue and cyan bars at the top show the harmonics of the time domain pulses number $m_1 = 0$ and $m_2 = 3$, respectively. At frequencies where these bars match, i.e., frequencies providing approximate solutions to Eq. (1), the alloharmonics of the $\Delta m = m_2 - m_1 = 3$ series with fringe separations of $\Delta\omega \approx \omega_0/3$ appear (the small black and red circles represent $\Delta n = 1$ and $\Delta n = 2$, respectively). These and other interferences are indicated by vertical dashed lines, with black lines representing interharmonic separation $\Delta n = 1$ and red lines representing $\Delta n = 2$.



Ext. Fig. 4. **Alloharmonic generation by a nonperiodic driver according to the nonlinear phase model, Eqs. (2), (4), with the cubic phase $\Phi(t) = \omega_0 t \left(1 + \beta \left(\frac{t}{T_0}\right)^2\right)$ and other model parameters as in Fig. 2: $\delta n = 0.25, n_{\max} = 200, a_n = 1, \phi_n = -[(n - 100)/75]^2$, and Gaussian envelope $A_\tau(t) = e^{-\frac{t^2}{\tau^2}}, \tau = 3T_0$.** **a**, Spectrum for $\beta = -0.0015$; the grey vertical lines show positions of ideal harmonics, $(n + \delta n)\omega_0$. **b**, Variation of the spectrum with β ; the dashed orange line ω_{\min} and dashed green line ω^* denote the onset and dominant region of the alloharmonics, respectively; these frequencies for $\beta = -0.0015$ are also shown in **a**. Solid lines show some of the alloharmonics with indicated interharmonic separations Δn and pulse separations Δm corresponding to fringe separations $\Delta\omega \approx \omega_0/\Delta m$. The purple dotted line shows alloharmonics $\Delta m = 1$ with fringe separation $\Delta\omega \approx \omega_0$.



Ext. Fig. 5. **Fits (red) of the experimental BISER spectrum (black) with (a) alloharmonic model and (b) harmonic model.** Error bars in the experimental spectrum are estimated standard deviations including the spectrograph's CCD dark current, readout, and shot noise. Error bars of the fit parameters in the left table are the fit standard errors⁶⁹. Error bars of the derived parameters in the right table are calculated by the error propagation⁷¹ taking into account the covariance matrix of the fit parameters.

Extended Data Table 1. Predicted parameters of alloharmonics in radio spectra of pulsars

Pulsar	Age, years	ν_0 , Hz	$\dot{\nu}$, Hz ²	α	τ , s	N_p	n_{\min}	ν_{\min} , MHz	R_{\min}	α_E	α_{L2}
J0835-4510 Vela	1.13×10^4	11.1946	-1.5666×10^{-11}	-6.25×10^{-14}	205	2300	3.48×10^9	38.9×10^3	8.00×10^{12}	-5.05×10^{-12}	-8.94×10^{-13}
Vela, 2016 glitch				$+2.32 \times 10^{-9}$	4.4	49	4.39×10^6	49	2.15×10^8		
J0633+1746 Geminga	3.42×10^5	4.2176	-1.9516×10^{-13}	-5.49×10^{-15}	205	864	1.05×10^{11}	445×10^3	9.12×10^{13}	-1.34×10^{-11}	-2.37×10^{-12}

J1808-2024 SGR 1806- 20	218	0.13234	-9.62 $\times 10^{-12}$	-2.75 $\times 10^{-10}$	204	27	6.74×10^7	8.92	1.82×10^9	-4.27 $\times 10^{-10}$	-7.56 $\times 10^{-11}$
Same, shorter time	-/-	-/-	-/-	-/-	15	2	9.10×10^8	120	-/-	-/-	-/-
J162759.5- 523504.3		0.000916	-5.04 $\times 10^{-16}$	-3.00 $\times 10^{-10}$	3274	3	5.56×10^8	0.509	1.67×10^9	-6.17 $\times 10^{-8}$	-1.09 $\times 10^{-8}$

ν_0 and $\dot{\nu}$: Pulsar rotation frequency and its time derivative (data from Ref.⁴³ for all rows except the bottom row and Ref.⁷² for the bottom row), α : dimensionless chirp parameter, τ and N_p : observation time window and number of periods in this window, n_{\min} and ν_{\min} : minimum harmonic order and frequency above which alloharmonics appear, R_{\min} : required resolving power to observe alloharmonics, α_E and α_{L2} : largest possible dimensionless chirp parameters of alloharmonics caused by the Earth's rotation and orbit at the L2 Sun-Earth Lagrange point (Supplemental Note 4).

References

- 1 Corkum, P. B. Plasma perspective on strong field multiphoton ionization. *Phys. Rev. Lett.* **71**, 1994-1997, doi:10.1103/PhysRevLett.71.1994 (1993).
- 2 Teubner, U. & Gibbon, P. High-order harmonics from laser-irradiated plasma surfaces. *Rev. Mod. Phys.* **81**, 445-479, doi:10.1103/RevModPhys.81.445 (2009).
- 3 Mills, C. & Fairhurst, S. Measuring gravitational-wave higher-order multipoles. *Phys. Rev. D* **103**, 024042, doi:10.1103/PhysRevD.103.024042 (2021).
- 4 Centrella, J., Baker, J. G., Kelly, B. J. & van Meter, J. R. Black-hole binaries, gravitational waves, and numerical relativity. *Rev. Mod. Phys.* **82**, 3069-3119, doi:10.1103/RevModPhys.82.3069 (2010).
- 5 Reichert, J., Holzwarth, R., Udem, T. & Hänsch, T. W. Measuring the frequency of light with mode-locked lasers. *Opt. Comm.* **172**, 59-68, doi:10.1016/S0030-4018(99)00491-5 (1999).
- 6 Jones, D. J. *et al.* Carrier-Envelope Phase Control of Femtosecond Mode-Locked Lasers and Direct Optical Frequency Synthesis. *Science* **288**, 635-639, doi:doi:10.1126/science.288.5466.635 (2000).
- 7 Strickland, D. & Mourou, G. Compression of amplified chirped optical pulses. *Opt. Comm.* **55**, 447-449, doi:10.1016/0030-4018(85)90120-8 (1985).
- 8 Esirkepov, T. Z., Bulanov, S. V., Kando, M., Pirozhkov, A. S. & Zhidkov, A. G. Boosted High-Harmonics Pulse from a Double-Sided Relativistic Mirror. *Phys. Rev. Lett.* **103**, 025002-025004, doi:10.1103/PhysRevLett.103.025002 (2009).
- 9 Behmke, M. *et al.* Controlling the Spacing of Attosecond Pulse Trains from Relativistic Surface Plasmas. *Phys. Rev. Lett.* **106**, 185002 (2011).
- 10 Borot, A. *et al.* Attosecond control of collective electron motion in plasmas. *Nature Phys.* **8**, 416-421, doi:10.1038/nphys2269 (2012).
- 11 Kim, I. J. *et al.* Relativistic frequency upshift to the extreme ultraviolet regime using self-induced oscillatory flying mirrors. *Nat Commun* **3**, 1231, doi:10.1038/ncomms2245 (2012).
- 12 Pirozhkov, A. S. *et al.* Soft-X-Ray Harmonic Comb from Relativistic Electron Spikes. *Phys. Rev. Lett.* **108**, 135004-135005, doi:10.1103/PhysRevLett.108.135004 (2012).
- 13 Pirozhkov, A. S. *et al.* Burst intensification by singularity emitting radiation in multi-stream flows. *Scientific Reports* **7**, 17968 (17910 pages), doi:10.1038/s41598-017-17498-5 (2017).
- 14 Boyle, M. *et al.* The SXS collaboration catalog of binary black hole simulations. *Classical and Quantum Gravity* **36**, 195006, doi:10.1088/1361-6382/ab34e2 (2019).
- 15 *SXS Gravitational Waveform Database*, <<https://data.black-holes.org/waveforms/index.html>> (accessed on 23 Apr 2021).
- 16 Udem, T., Holzwarth, R. & Hansch, T. W. Optical frequency metrology. *Nature* **416**, 233-237 (2002).

- 17 Picqué, N. & Hänsch, T. W. Frequency comb spectroscopy. *Nat. Photon* **13**, 146-157, doi:10.1038/s41566-018-0347-5 (2019).
- 18 Bulanov, S. V., Naumova, N. M. & Pegoraro, F. Interaction of an Ultrashort, Relativistically Strong Laser-Pulse with an Overdense Plasma. *Phys. Plasmas* **1**, 745-757, doi:10.1063/1.870766 (1994).
- 19 Lichters, R., Meyer - ter - Vehn, J. & Pukhov, A. Short - pulse laser harmonics from oscillating plasma surfaces driven at relativistic intensity. *Phys. Plasmas* **3**, 3425-3437, doi:10.1063/1.871619 (1996).
- 20 Farkas, G. & Tóth, C. Proposal for attosecond light pulse generation using laser induced multiple-harmonic conversion processes in rare gases. *Phys. Lett. A* **168**, 447-450, doi:10.1016/0375-9601(92)90534-S (1992).
- 21 Paul, P. M. *et al.* Observation of a Train of Attosecond Pulses from High Harmonic Generation. *Science* **292**, 1689-1692, doi:10.1126/science.1059413 (2001).
- 22 Nomura, Y. *et al.* Attosecond phase locking of harmonics emitted from laser-produced plasmas. *Nature Phys.* **5**, 124-128, doi:10.1038/nphys1155 (2009).
- 23 Pirozhkov, A. S. *et al.* Generation of high-energy attosecond pulses by the relativistic-irradiance short laser pulse interacting with a thin foil. *Phys. Lett. A* **349**, 256-263, doi:10.1016/j.physleta.2005.09.024 (2006).
- 24 Savage, R. L., Joshi, C. & Mori, W. B. Frequency upconversion of electromagnetic radiation upon transmission into an ionization front. *Phys. Rev. Lett.* **68**, 946-949, doi:10.1103/PhysRevLett.68.946 (1992).
- 25 Koga, J. K. *et al.* Fixed blueshift of high intensity short pulse lasers propagating in gas chambers. *Phys. Plasmas* **7**, 5223-5231, doi:10.1063/1.1320469 (2000).
- 26 Wilks, S. C., Dawson, J. M., Mori, W. B., Katsouleas, T. & Jones, M. E. Photon accelerator. *Phys. Rev. Lett.* **62**, 2600-2603, doi:10.1103/PhysRevLett.62.2600 (1989).
- 27 Murphy, C. D. *et al.* Evidence of photon acceleration by laser wake fields. *Phys. Plasmas* **13**, 033108, doi:10.1063/1.2178650 (2006).
- 28 Streeter, M. J. V. *et al.* Characterization of laser wakefield acceleration efficiency with octave spanning near-IR spectrum measurements. *Phys. Rev. Accel. Beams* **25**, 101302, doi:10.1103/PhysRevAccelBeams.25.101302 (2022).
- 29 Bulanov, S. V., Inovenkov, I. N., Kirsanov, V. I., Naumova, N. M. & Sakharov, A. S. Nonlinear Depletion of Ultrashort and Relativistically Strong Laser-Pulses in an Underdense Plasma. *Phys. Fluids B* **4**, 1935-1942, doi:10.1063/1.860046 (1992).
- 30 Shadwick, B. A., Schroeder, C. B. & Esarey, E. Nonlinear laser energy depletion in laser-plasma accelerators. *Phys. Plasmas* **16**, 056704-056708 (2009).
- 31 Esarey, E., Schroeder, C. B. & Leemans, W. P. Physics of laser-driven plasma-based electron accelerators. *Rev. Mod. Phys.* **81**, 1229-1285, doi:10.1103/RevModPhys.81.1229 (2009).
- 32 Corde, S. *et al.* Femtosecond x rays from laser-plasma accelerators. *Rev. Mod. Phys.* **85**, 1-48 (2013).
- 33 Nie, Z. *et al.* Photon deceleration in plasma wakes generates single-cycle relativistic tunable infrared pulses. *Nature Communications* **11**, 2787, doi:10.1038/s41467-020-16541-w (2020).
- 34 Abbott, B. P. *et al.* Observation of Gravitational Waves from a Binary Black Hole Merger. *Phys. Rev. Lett.* **116**, 061102, doi:10.1103/PhysRevLett.116.061102 (2016).
- 35 Beskin, V. S. Radio pulsars: already fifty years! *Physics-Uspokhi* **61**, 353, doi:10.3367/UFNe.2017.10.038216 (2018).
- 36 Malov, I. F. & Marozava, H. P. On Braking Mechanisms in Radio Pulsars. *Astronomy Reports* **66**, 25-31, doi:10.1134/S106377292202007X (2022).

- 37 Palfreyman, J., Dickey, J. M., Hotan, A., Ellingsen, S. & van Straten, W. Alteration of the magnetosphere of the Vela pulsar during a glitch. *Nature* **556**, 219-222, doi:10.1038/s41586-018-0001-x (2018).
- 38 Malvache, A., Borot, A., Quéré, F. & Lopez-Martens, R. Coherent wake emission spectroscopy as a probe of steep plasma density profiles. *Phys. Rev. E* **87**, 035101, doi:10.1103/PhysRevE.87.035101 (2013).
- 39 Chen, Z., Yan, M., Hänsch, T. W. & Picqué, N. A phase-stable dual-comb interferometer. *Nature Communications* **9**, 3035, doi:10.1038/s41467-018-05509-6 (2018).
- 40 Skordis, C. & Złótnik, T. New Relativistic Theory for Modified Newtonian Dynamics. *Phys. Rev. Lett.* **127**, 161302, doi:10.1103/PhysRevLett.127.161302 (2021).
- 41 Hewish, A., Bell, S. J., Pilkington, J. D. H., Scott, P. F. & Collins, R. A. Observation of a Rapidly Pulsating Radio Source. *Nature* **217**, 709-713, doi:10.1038/217709a0 (1968).
- 42 Malofeev, V. M. & Tyul'bashev, S. A. Investigation of radio pulsar emission features using power spectra. *Research in Astronomy and Astrophysics* **18**, 096, doi:10.1088/1674-4527/18/8/96 (2018).
- 43 Manchester, R. N., Hobbs, G. B., Teoh, A. & Hobbs, M. The Australia Telescope National Facility Pulsar Catalogue. *The Astronomical Journal* **129**, 1993, doi:10.1086/428488 (2005).
- 44 Malofeev, V. M. & Malov, O. I. Detection of Geminga as a radio pulsar. *Nature* **389**, 697-699, doi:10.1038/39530 (1997).
- 45 Popmintchev, T. *et al.* Bright Coherent Ultrahigh Harmonics in the keV X-ray Regime from Mid-Infrared Femtosecond Lasers. *Science* **336**, 1287-1291, doi:10.1126/science.1218497 (2012).
- 46 Dromey, B. *et al.* Bright Multi-keV Harmonic Generation from Relativistically Oscillating Plasma Surfaces. *Phys. Rev. Lett.* **99**, 85001, doi:10.1103/PhysRevLett.99.085001 (2007).
- 47 Xu, B., Fan, X., Wang, S. & He, Z. Sub-femtometer-resolution absolute spectroscopy with sweeping electro-optic combs. *Opto-Electronic Advances* **5**, 210023, doi:10.29026/oea.2022.210023 (2022).
- 48 Kiriya, H. *et al.* Temporal contrast enhancement of petawatt-class laser pulses. *Opt. Lett.* **37**, 3363-3365, doi:10.1364/OL.37.003363 (2012).
- 49 Moulet, A., Grabielle, S., Cornaggia, C., Forget, N. & Oksenhendler, T. Single-shot, high-dynamic-range measurement of sub-15 fs pulses by self-referenced spectral interferometry. *Opt. Lett.* **35**, 3856-3858 (2010).
- 50 Pirozhkov, A. S. *et al.* Approaching the diffraction-limited, bandwidth-limited Petawatt. *Opt. Express* **25**, 20486-20501, doi:10.1364/oe.25.020486 (2017).
- 51 Askaryan, G. A. Effect of the gradient of a strong electromagnetic ray on electrons and atoms. *Zhur. Eksptl'. i Teoret. Fiz.* **42**, 1567-1570 (1962).
- 52 Litvak, A. Finite-amplitude wave beams in a magnetoactive plasma. *Sov. Phys. JETP*. **30**, 344 (1970).
- 53 Sun, G.-Z., Ott, E., Lee, Y. C. & Guzdar, P. Self-focusing of short intense pulses in plasmas. *Phys. Fluids* **30**, 526-532, doi:10.1063/1.866349 (1987).
- 54 Pirozhkov, A. S. *et al.* High order harmonics from relativistic electron spikes. *New J. Phys.* **16**, 093003-093030, doi:10.1088/1367-2630/16/9/093003 (2014).
- 55 Mourou, G. A., Tajima, T. & Bulanov, S. V. Optics in the relativistic regime. *Rev. Mod. Phys.* **78**, 309-371, doi:10.1103/RevModPhys.78.309 (2006).
- 56 Jackson, J. D. *Classical Electrodynamics*. 3rd edn, (John Wiley & Sons, 1998).
- 57 Bulanov, S. S. *et al.* Generation of GeV protons from 1 PW laser interaction with near critical density targets. *Phys. Plasmas* **17**, 043105-043108, doi:10.1063/1.3372840 (2010).
- 58 Akhiezer, A. & Polovin, R. Theory of wave motion of an electron plasma. *Sov. Phys. JETP* **3**, 696 (1956).
- 59 Esirkepov, T. Z., Kato, Y. & Bulanov, S. V. Bow Wave from Ultraintense Electromagnetic Pulses in Plasmas. *Phys. Rev. Lett.* **101**, 265001-265004, doi:10.1103/PhysRevLett.101.265001 (2008).

- 60 Luo, J. *et al.* Dynamics of boundary layer electrons around a laser wakefield bubble. *Phys. Plasmas* **23**, 103112, doi:10.1063/1.4966047 (2016).
- 61 Ning, L., Jie, M. & Fancun, K. Numerical Studies on Bow Waves in Intense Laser-Plasma Interaction. *Laser Part. Beams* **2023**, 9414451, doi:10.1155/2023/9414451 (2023).
- 62 Tajima, T. & Dawson, J. Laser electron accelerator. *Phys. Rev. Lett.* **43**, 267-270, doi:10.1103/PhysRevLett.43.267 (1979).
- 63 Arnold, V. I. *Catastrophe theory*. 3rd edn, (Springer-Verlag, 1992).
- 64 Poston, T. & Stewart, I. *Catastrophe theory and its applications*. (Dover Pubns, 1996).
- 65 Pirozhkov, A. S. *et al.* Laser Requirements for High-Order Harmonic Generation by Relativistic Plasma Singularities. *Quantum Beam Sci.* **2**, 7, doi:10.3390/qubs2010007 (2018).
- 66 Ralchenko, Y., Kramida, A. E., Reader, J. & Team, N. A. *NIST Atomic Spectra Database (ver. 4.0.1)*, <<http://physics.nist.gov/asd>> (accessed on 24-Mar 2011).
- 67 Henke, B. L., Gullikson, E. M. & Davis, J. C. X-Ray Interactions: Photoabsorption, Scattering, Transmission, and Reflection at E = 50-30,000 eV, Z = 1-92. *At. Data Nucl. Data Tables* **54**, 181-342, doi:10.1006/adnd.1993.1013 (1993, available online at http://henke.lbl.gov/optical_constants/).
- 68 Gullikson, E. *X-Ray Interactions With Matter*, <https://henke.lbl.gov/optical_constants/> (accessed on 29-Nov 2022).
- 69 OriginPro v. 2022b 9.9.5.167 (OriginLab, 2022).
- 70 Ajith, P. *et al.* Data formats for numerical relativity waves. *arXiv*, 0709.0093v0703, doi:10.48550/arXiv.0709.0093 (2011).
- 71 Mathematica v. 13.1.0.0 (Wolfram Research, 2022).
- 72 Hurley-Walker, N. *et al.* A radio transient with unusually slow periodic emission. *Nature* **601**, 526-530, doi:10.1038/s41586-021-04272-x (2022).